

Aerosol Vertical Mass Flux Measurements During Heavy Aerosol Pollution Episodes at a Rural Site and an Urban Site in the Beijing Area of the North China Plain

Renmin Yuan¹, Xiaoye Zhang^{2,4}, Hao Liu¹, Yu Gui¹, Bohao Shao¹, Xiaoping Tao⁵, Yaqiang Wang², Junting Zhong²,
Yubin Li³ and Zhiqiu Gao³

¹School of Earth and Space Sciences, University of Science and Technology of China, Anhui, 230026, China

²State Key Laboratory of Severe Weather & Key Laboratory of Atmospheric Chemistry of CMA, Chinese Academy
of Meteorological Sciences, Beijing 100081, China

³School of Geography and Remote Sensing, Nanjing University of Information Science and Technology, Nanjing
210044, China

⁴Center for Excellence in Regional Atmospheric Environment, IUE, CAS, Xiamen 361021, China.

⁵School of Physical Sciences, University of Science and Technology of China, Anhui, 230026, China

Correspondence: Renmin Yuan (rmyuan@ustc.edu.cn) and Xiaoye Zhang (xiaoye@cma.gov.cn)

Abstract:

Due to excessive anthropogenic emissions, heavy aerosol pollution episodes (HPEs) often occur during winter in the Beijing-Tianjin-Hebei (BTH) area of the North China Plain. Extensive observational studies have been carried out to understand the causes of HPEs; however, few measurements of vertical aerosol fluxes exist, despite them being the key to understanding vertical aerosol mixing, specifically during weak turbulence stages in HPEs. In the winter of 2016 and the spring of 2017 aerosol vertical mass fluxes were measured by combining large aperture scintillometer (LAS) observations, surface PM_{2.5} and PM₁₀ mass concentrations, and meteorological observations, including temperature, relative humidity (RH), and visibility, at a rural site in Gucheng (GC), Hebei Province, and an urban site at the Chinese Academy of Meteorological Sciences (CAMS) in Beijing located 100 km to the northeast. These are based on the light propagation theory and surface-layer similarity theory. The near-ground aerosol mass flux was generally lower in winter than in spring and weaker in rural GC than in urban Beijing. This finding provides direct observational evidence for a weakened turbulence intensity and low vertical aerosol fluxes in winter and polluted areas such as GC. The HPEs included a transport stage (TS), an accumulative stage (AS), and a removal stage (RS). During the HPEs from 25 January 2017 to January 31, 2017, in Beijing, the mean mass flux decreased by 51% from 0.0049 mg m⁻²s⁻¹ in RSs to 0.0024 mg m⁻²s⁻¹ in the TSs. During the ASs, the mean mass flux decreased further to 0.00087 mg m⁻²s⁻¹, accounting for approximately 1/3 of the flux in the TSs. A similar reduction from the TSs to ASs was observed in the HPE from 16 December 2016 to 22 December 2016 in GC. It can be seen that from the TS to the AS, the aerosol vertical turbulent flux decreased, but the aerosol particle concentration within surface layer increased, and it is inferred that in addition to the contribution of regional transport from upwind areas during the TS, suppression of vertical turbulence mixing confining aerosols to a

38 shallow boundary layer increased accumulation.

39 **1 Introduction**

40 Recently, due to the country's rapid development of industrialization and urbanization, China
41 has experienced heavy aerosol pollution episodes, particularly in the Beijing, Tianjin and Hebei
42 (BTH) region, which is one of the most polluted areas in China (Zhang et al., 2012). The pollution
43 episodes often last for a long duration in the BTH region and cover a wide area, particularly in
44 winter; they also severely reduce near-ground visibility (Lei and Wuebbles, 2013) and can have
45 detrimental effects on public health (He et al., 2018; Cao et al., 2012). This heavy pollution
46 environment has received extensive attention in recent years, and many observational studies have
47 been carried out (Zhong et al., 2018b; Sun et al., 2014; Wang et al., 2015; Guo et al., 2011; Zhang
48 et al., 2009b; Huang et al., 2014). Modelling studies have also been performed to examine the
49 regional transport of pollutants (Wang et al., 2014) and to study the important role of large-eddy
50 convective turbulent mixing in the vertical transfer of pollutants from a field campaign in Beijing
51 (Li et al., 2018). However, few study on the turbulence contribution of the aerosol turbulent flux in
52 the surface layer has been conducted.

53 Ground pollutant emissions are known as the main source of aerosols in the atmosphere.
54 However, in previous studies, no measurements of ground emissions during heavy pollution events
55 were collected. Surface emission data are currently required for model verification and pollution
56 predictions, and these data are primarily obtained through emission inventories (Wu et al., 2012;
57 Bond et al., 2004). The establishment of emission inventories is primarily based on emission activity
58 and emission factor (EF) data (Akagi et al., 2011; Lu et al., 2011; Roden et al., 2006; Zhang and
59 Tao, 2009). Emissions data are mainly obtained from statistical yearbooks (Zhang et al., 2009a).
60 Some studies have used fixed EFs while others have implemented dynamic EFs (Bond et al., 2004;
61 Zhang et al., 2009a). Many factors are considered in dynamic EFs, such as the size of a city, the
62 degree of economic development, the type of fuel, the kind of technology, product energy
63 consumption, the control technology, and so on, as well as estimates based on actual measured
64 meteorological parameters and aerosol parameters (Chen et al., 2015; Karvosenoja et al., 2008; Shen
65 et al., 2013). A numerical model has also been used to estimate average fleet emission factors in
66 typical urban conditions (Ketzler et al., 2003; Krecl et al., 2018). The uncertainties in the emissions
67 of primary aerosols for inventories are high due to the highly uncertain contributions from the
68 residential sector (Li et al., 2017), and the error in aerosol fluxes based on the use of emission
69 inventories is huge (Liu et al., 2017; Zheng et al., 2017). Emission inventories constructed using the
70 EF method provide only the total emission amount of atmospheric pollutants within a region.
71 However, the emission data should be gridded to a suitable scale for air quality modeling and
72 pollution predictions. Thus, near-surface aerosol emission data with a higher temporal and spatial
73 resolution are urgently needed.

74 Many methods have been used to obtain aerosol flux data. For the upward transport of aerosols
75 near the surface layer, the aerodynamic approach was adopted in the early years. The aerosol
76 concentration gradient at different heights was measured and then calculated based on the similarity
77 theory of the near-surface layer or calculated by the boundary layer box model, which can be based
78 on meteorological data (Ceburnis et al., 2016; Hourdin et al., 2015; Zhang and Li, 2014). The
79 emission rates of bioaerosols were also estimated from spore counts and molecular tracers (Elbert
80 et al., 2007). The abundance of microbes and meteorological data were measured, and an estimate

81 may be derived from the sea-air exchange of microorganisms (Mayol et al., 2014).

82 With the use of instruments for measuring the number of aerosol particles (for example, a
83 condensational particle counter, abbreviated as CPC by TSI), the eddy covariance (EC) method has
84 been applied, and measurements of the aerosol particle number flux have become possible (Buzorius
85 et al., 1998). The vertical turbulent flux of the aerosol particle number density F_p is denoted as a
86 cross-covariance between the aerosol particle number concentration N' and the vertical wind speed
87 w' (Ripamonti et al., 2013). To obtain vertical turbulent flux of the aerosol number density, the EC
88 principle allows quantifying the number flux from fluctuation measurements. As a result, the
89 vertical turbulent flux of the aerosol particle number density has been measured in many cities, such
90 as in Toronto, Canada (Gordon et al., 2011), Stockholm, Sweden (Vogt et al., 2011b), Helsinki,
91 Finland (Ripamonti et al., 2013), London, UK (Harrison et al., 2012), the Blodgett Forest
92 Observatory in the United States (Farmer et al., 2011), and measurements of sea salt aerosol fluxes
93 in northern Europe (Brooks et al., 2009; Sproson et al., 2013). These results have shown the
94 quantitative relationship among urban aerosol fluxes, urban vehicle emissions, and meteorological
95 conditions (Jarvi et al., 2009) and have been used to determine transport characteristics of sea salt
96 aerosol and provide further knowledge of aerosol properties (Nemitz et al., 2009). These
97 measurements have been mainly collected in cities because of their anthropogenic contributions to
98 aerosol emissions. These data can be used as routine model inputs. Direct eddy covariance
99 measurements of aerosol exchanges in tropical forests, where primary biological aerosol particles
100 represent a substantial fraction of the airborne particulate matter (Graham et al., 2003), were also
101 performed by Ahlm et al. (Ahlm et al., 2010a; Ahlm et al., 2010b) and Whitehead et al. (Whitehead
102 et al., 2010), potentially giving a proxy for microbial emissions in tropical ecosystems.

103 Although measurements of urban aerosol particle number density fluxes have been collected,
104 the current eddy covariance method only provides fluxes for the aerosol particle number density at
105 a point. We know that the underlying surface of a city is very complex, and thus the aerosol particle
106 flux is not homogeneous in the horizontal. For a complex underlying surface such as a city, these
107 point measurements are not representative of wider area. Therefore, it is of great importance to
108 design an aerosol flux measurement system with larger spatial representation.

109 The use of eddy covariance principles to measure sensible heat fluxes has been widely
110 performed (Lee, 2004). Current sensible heat fluxes can also be obtained using a large aperture
111 scintillometer (LAS) based on the light propagation theory and atmospheric surface layer similarity
112 theory (Zeweldi et al., 2010). This configuration makes it possible to achieve aerosol mass flux
113 measurements using the same principles. Recently, we measured the imaginary part of the
114 atmospheric equivalent refractive index structure parameter based on the light propagation theory
115 (Yuan et al., 2015). The results showed that the imaginary part of the atmospheric equivalent
116 refractive index structure parameter is related to turbulent transport and the spatial distribution
117 characteristics of aerosols. Experiments also showed that there is a strong correlation between the
118 imaginary part of the atmospheric equivalent refractive index and the mass concentration of aerosol
119 particles (Yuan et al., 2016). Thus, similar to the temperature structure parameter reflecting the
120 sensible heat flux, the structural parameter of the imaginary part of the atmospheric equivalent
121 refractive index can reveal the mass flux of aerosol particles. This paper attempts to measure the
122 aerosol mass flux in the BTH area, especially during heavy aerosol pollution episodes.

123 Generally, based on the $PM_{2.5}$ daily mean mass concentration limit in the primary standard of
124 China's national environmental quality standards (EPD, 2012), a pollution episode is referred to as

125 the period during which the PM_{2.5} concentration exceeds 80 $\mu\text{g m}^{-3}$ for 3 consecutive days between
126 two clean periods, while a period when the PM_{2.5} level is less than 35 $\mu\text{g m}^{-3}$ is defined as a clean
127 period. Pollution episodes with peak PM_{2.5} values of more than 400 $\mu\text{g m}^{-3}$ or less than 300 $\mu\text{g m}^{-3}$
128 are termed heavy-pollution episodes (HPEs) or light-pollution episodes (LPEs), respectively (Zhong
129 et al., 2017b).

130 To gain a deeper understanding of the interaction between atmospheric heavy pollution and
131 weather in the BTH region, joint observations have been carried out in the BTH region since the
132 winter of 2016 (Zhong et al., 2018c; Zhong et al., 2018b; Wang et al., 2018; Shen et al., 2018). Based
133 on meteorological causes of the increase or decrease in PM_{2.5} mass concentrations, an HPE in the
134 BTH region can be divided into a transport stage (TS), an accumulative stage (AS) and a removal
135 stage (RS). During the TS, the PM_{2.5} high concentration levels are caused by relatively strong
136 southerly winds, which carry polluted air masses from more populated southern industrial regions
137 (Guo et al., 2014; Zhong et al., 2018a). Before elevation of PM_{2.5} concentrations during TSs, the
138 urban PM_{2.5} mass concentration of Baoding, which is typically representative of pollution conditions
139 in the south of Beijing, was much higher than Beijing; the winds in Beijing rapidly shifted from
140 northerly to southerly. Then the rising in PM_{2.5} occurred, consistently with southerly slight or gentle
141 breezes in the BL. The southerly air mass moves more than 288 km d^{-1} below 500 m (estimated
142 from the measured wind speed), which are fast enough to transport pollutants to Beijing. Such
143 processes indicate southerly pollutant transport is primarily responsible for elevation of PM_{2.5}
144 concentrations, given the pollution transport pathway of the southwest wind belt determined by the
145 unique geographic features of the North China Plain, with the Tai-hang Mountains and the Yan
146 Mountains strengthening the southwest wind belt and leading the convergence of pollutant transport
147 in Beijing (Su et al., 2004). During the ASs, PM_{2.5} increase is dominated by stable atmospheric
148 stratification characteristic of southerly slight or calm winds, near-ground anomalous inversion, and
149 moisture accumulation. When aerosol particles by vertical transport are accumulated to a certain
150 degree, the dominant scattering aerosols will substantially back-scatter solar radiation, causing a
151 reduction in the amount of solar radiation that reaches the surface, which creates a near-ground
152 cooling effect resulting in the lack of vertical mixing in the near-surface layer. (Zhong et al., 2018c).
153 A feedback effect of further worsened meteorological conditions aggravates PM_{2.5} pollution (Zhong
154 et al., 2017a). During the RSs, strong north-westerly winds whose velocity increases with height
155 occur predominantly. Strong northerly winds are from less populated north mountainous areas and
156 carry unpolluted air masses to Beijing, which is favorable for pollution dispersion. The observations
157 reveal the large-scale and mesoscale transport processes of aerosols between HPEs in the BTH
158 region in the winter of 2016. However, during HPEs, no research has been conducted in the BTH
159 area on quantifying the contribution of surface emissions to the concentration of pollutants. In this
160 study, we focus on aerosol emission during HPEs through field observations of aerosol turbulent
161 based on the light propagation theory and surface similarity in the Beijing urban district and
162 Gucheng suburban area.

163 The second section of this paper introduces the theory of aerosol vertical turbulent flux
164 measurements, the third section introduces the experiment, the fourth section gives the experimental
165 results, and finally, the conclusion and discussion are presented in the fifth section.

166 2 Theory and methods

167 The principles for calculating the vertical flux of aerosol particles and the approach for
168 calculating the friction velocity and characteristic temperature using the temperature and wind
169 profiles is presented in the following subsections.

170 2.1 Calculation of the aerosol mass vertical flux

171 According to the micrometeorological principle (Stull, 1988), similar to the estimation method
172 of the sensible heat flux, the aerosol flux F_a can be obtained as follows:

$$173 \quad F_a = u_* M_* \quad (1)$$

174 where u_* is the friction velocity, which can be obtained from the temperature and wind speed
175 profiles or directly from three-dimensional wind speed measurements; see Sec. 2.2. Prior
176 experiments have shown that the spectral characteristics of aerosol number concentration
177 fluctuations approximate the spectral characteristics of molecular density fluctuations. (Martensson
178 et al. 2006; Vogt et al. 2011b). Therefore, aerosol particles can be approximated as scalars for
179 turbulent statistics, and characteristic parameters M_* similar to the scalars can be introduced,
180 which can be regarded as the atmospheric aerosol mass concentration scale in the surface layer and
181 deduced from surface layer similarity theory. This approximation is similar to the surface-layer
182 temperature scale (Stull, 1988) as follows:

$$183 \quad \frac{C_M^2 (z-d)^{2/3}}{M_*^2} = \eta(\xi) \quad (2)$$

184 where z is the measurement height, d is the zero-displacement height (Evans and De Bruin, 2011;
185 Hartogensis et al., 2003), $\xi=(z-d)/L$ is the nondimensional stability parameter, L is the Monin-
186 Obukhov (MO) length and defined as $L = \frac{\bar{T} u_*^2}{\kappa g T_*}$ (Stull, 1988), \bar{T} is the average temperature, T_*
187 is the surface-layer characteristic temperature, κ is the von Karman constant, which is 0.4, and g is
188 acceleration due to gravity. The stability function ($\eta(\xi)$) can be expressed as follows depending
189 on the stability condition (DeBruin et al., 1995):

$$190 \quad \eta(\xi) = a_1 [1 - a_2 \xi]^{-2/3} \quad (3)$$

191 for unstable conditions ($\xi < 0$), and the following:

192
$$\eta(\xi) = b_1[1 + b_2(\xi)^{e_1}] \quad (4)$$

193 for stable conditions ($\zeta \geq 0$) (Wyngaard et al., 1971).

194 In Eqs. (3) and (4), a_1, a_2, b_1, b_2 and e_1 are constants, and different experiments have provided
 195 different values, although the differences between these results are small. It is assumed that the
 196 aerosol mass concentration fluctuation characteristics are the same as the temperature fluctuation
 197 characteristics and the same similarity law of Eq. (2) is satisfied. Therefore, based on the

198 experimental data, the values of $\sqrt{\frac{C_T^2(z-d)^{2/3}}{\eta(\zeta)}}$ and T_* are calculated using various schemes.

199 After comparing the differences between the two, the scheme of DeBruin et al (DeBruin et al., 1995)
 200 with $a_1=4.9, a_2=9, b_1=5,$ and $b_2=0$ is taken based on minimal difference using the experimental data
 201 of this study.

202 C_M^2 in Eq. (2) is the aerosol mass concentration structure parameter. We assume that the
 203 aerosol particles in the atmosphere follow the movement of the air and satisfy the turbulent motion
 204 law. Previous studies have shown that the particle concentration fluctuation spectra follow a ‘-5/3’
 205 power law under unstable stratification conditions (Martensson et al., 2006; Vogt et al., 2011b), and
 206 the velocity-concentration co-spectra follows a ‘-4/3’ power law (Martensson et al., 2006; Vogt et
 207 al., 2011a; Kaimal et al., 1972). Thus, similarity of atmospheric aerosols and temperature can be
 208 assumed for the purpose. Then, at a separation (r) of the order in the inertial subrange in a locally
 209 isotropic field, the aerosol mass concentration (denoted as M_a) structure function ($D_M(r)$) follows a
 210 “2/3 law” (Wyngaard, 2010) and can be expressed as $D_M(r) = \overline{[M_a(\mathbf{x}) - M_a(\mathbf{x} + \mathbf{r})]^2} = C_M^2 r^{2/3}$,
 211 where \mathbf{x} is the position vector, \mathbf{r} is the separation vector, and the overbar indicates the spatial average.

212 The following describes the method to deduce the aerosol mass concentration structure
 213 parameter C_M^2 .

214 Although the aerosol particles are dispersed in the air, the macroscopic behavior of the gas-
 215 particle two-phase mixture is the same as if it is perfectly continuous in structure and physical
 216 quantities, such as the mass and refractive index associated with the matter contained within a given
 217 small volume, which will be regarded as being spread continuously over that volume. The aerosol
 218 particles and gases in the atmosphere can be considered as an equivalent medium, and an
 219 atmospheric equivalent refractive index (AERI) n_{equ} is introduced that contains the real part n_{re} and
 220 the imaginary part n_{im} of the equivalent refractive index. Thus, $n_{equ} = n_{re} + i \cdot n_{im}$. For visible light, the
 221 attenuation of light by gases in the atmosphere is very weak; the cause of the attenuation is the

222 absorption and scattering due to aerosol particles. Therefore, the real part of the equivalent medium
 223 of aerosol particles and gases is determined by the gas composition of the air. The fluctuation of the
 224 real part is mainly determined by temperature fluctuations; the imaginary part is determined by the
 225 aerosol particles, and the fluctuation of the imaginary part is determined by fluctuations in the
 226 aerosol concentration.

227 For visible light, there is a robust linear relationship between the variation of the real part of

228 the AERI and the variation of the atmospheric temperature, namely, $R_{TN} = \frac{\delta T}{\delta n_{Re}}$; thus, we have the

229 following:

$$230 \quad R_{TN} = -1.29 \times 10^4 \times \left(1 + \frac{7.52 \times 10^{-3}}{\lambda^2}\right)^{-1} \frac{\bar{T}^2}{\bar{P}} \quad (5)$$

231 which is based on the relationship between the real part of the AERI (n_{Re}) and atmospheric
 232 temperature (Tatarskii, 1961). Because the wavelength is deterministic, the ratio R_{TN} can be obtained
 233 by measuring the atmospheric temperature. The imaginary part of the AERI (n_{Im}) has a close
 234 correspondence with the extinction coefficient of the equivalent medium, and the extinction
 235 coefficient is inversely proportional to the visibility. The light wavelength is selected as 0.620 μm .
 236 This wavelength is only weakly absorbed by O₃; therefore, the observed absorption is primarily due
 237 to aerosol (Brion et al., 1998; Lou et al., 2014; Nebuloni, 2005). Higher concentrations of aerosols
 238 in the atmosphere are related to lower visibility and vice versa; thus, the relationship between the
 239 imaginary part of the AERI and the atmospheric aerosol mass concentration can be established. The
 240 ratio of the atmospheric aerosol mass concentration to the imaginary part of the AERI R_{MN} can be
 241 defined as follows:

$$242 \quad R_{MN} = \frac{M_a}{n_{Im}}. \quad (6)$$

243 Theoretical analysis has revealed that R_{MN} is associated with the aerosol particle size
 244 distribution, mass density of the aerosol particles, and the aerosol particle refractive index. Because
 245 of the relatively small variations in particle size distributions and aerosol refractive index (Dubovik
 246 et al., 2002), R_{MN} can be treated as a constant for surface-layer aerosols at a given location. Of course,
 247 R_{MN} can be obtained by simultaneously measuring M_a and the imaginary part of the AERI, so that
 248 real-time R_{MN} can be obtained. M_a approximates the PM₁₀ value. The variable n_{im} can be calculated
 249 as follows (Yuan et al., 2016):

$$250 \quad n_{im} = \frac{0.55e-6}{4\pi} \cdot \frac{3.912}{L_v} \quad (7)$$

251 where the unit of visibility (L_V) is m.

252 According to Eqs. (5) and (6), we have the following:

$$253 \quad C_T^2 = R_{TN}^2 C_{n,Re}^2 \quad (8)$$

$$254 \quad C_M^2 = R_{MN}^2 C_{n,Im}^2 \quad (9)$$

255 Thus, the temperature structure parameter C_T^2 and the aerosol mass concentration fluctuation
256 structure parameter C_M^2 are converted into the measurement of the real and imaginary structural
257 parameters of the AERI, namely, $C_{n,Re}^2$ and $C_{n,Im}^2$ respectively.

258 The measurement of relevant parameters is performed based on the light propagation theory.
259 When light is transmitted in an equivalent medium, the AERI fluctuation will cause light
260 fluctuations in light intensity. When the attenuation caused by scattering and absorption along the
261 propagation path is very weak, light intensity fluctuation depends on the fluctuation of the real part
262 of the AERI along the propagation path. When the attenuation caused by scattering and absorption
263 along the propagation path is relatively strong, the light intensity fluctuation is also related to the
264 fluctuation of the imaginary part of the AERI along the propagation path. With the spectral analysis
265 method, the LAS light intensity fluctuations can be separated into the contributions of the real and
266 imaginary parts of the AERI. The contribution of the real part of the AERI corresponds to the high
267 frequencies, whereas the contribution of the imaginary part of the AERI corresponds to the low
268 frequencies, suggesting that the variances resulting from the real and imaginary parts are
269 independent. Therefore, the light intensity variances induced by the real and imaginary parts can be
270 detected separately at high frequencies and low frequencies from the LAS measurements (Yuan et
271 al., 2015). Thus, the real and imaginary structure parameters of the AERI can be calculated by our
272 developed LAS.

273 So far, we have completed the estimation of the aerosol mass turbulent flux.

274 According to the previous derivation and analysis, there are two calculation schemes for
275 determining the aerosol mass flux as follows:

$$276 \quad F_{a1} = \left(\frac{C_{n,Im}^2}{C_{n,Re}^2} \right)^{1/2} \frac{R_{MN}}{R_{TN}} u_* |T_*| \quad (10)$$

$$277 \quad F_{a2} = u_* \sqrt{\frac{C_M^2 (z-d)^{2/3}}{\eta(\xi)}} = u_* R_{MN} \sqrt{\frac{C_{n,Im}^2 (z-d)^{2/3}}{\eta(\xi)}} \quad (11)$$

278 When the free convection approximation ($-\xi \gg 1$) is assumed, based on the definition of the
 279 M-O length, and the similarity theory (Wyngaard et al., 1971), the following can be obtained:

$$280 \quad F_{a3} = a \left(\frac{g}{T} \right)^{1/2} R_{TN}^{1/2} (C_{n,Re}^2)^{1/4} R_{MN} (C_{n,Im}^2)^{1/2} (z-d) \quad (12)$$

281 where the coefficient $a = a_1^{-3/4} a_2^{1/2} \kappa^{1/2}$ can be taken as 0.567 (DeBruin et al., 1995; Lagouarde
 282 et al., 2006). Eqs. (10)-(12) are the theoretical basis for the aerosol mass flux measurements.

283 According to Eqs. (10)-(12), the vertical turbulent flux of aerosol particles is related to the
 284 strength of turbulent fluctuations of temperature and aerosol mass concentration fluctuations.

285 In this study, there is a weather tower in the north of Beijing. The weather tower is 6.1km far
 286 from the CAMS site. The meteorological observation data from the weather tower show that
 287 applicability of the Monin-Oubhov similarity theory under stable condition causes a significant error
 288 for T^* or u^* , while the Monin-Oubhov similarity theory is still basically applicable in the case of
 289 unstable stratification (Liu et al. 2009). In the roughness sub-layers of other cities, under the
 290 condition of unstable stratification, the local similarity theory is similar to MOST (Zou et al. 2018,
 291 2019). Because the height of the LAS instrument at the CAMS site was 43 m, during most of the
 292 time the conditions assumed for free convection were easily satisfied. During the day, the surface
 293 layer is usually unstable. At night, for the city, even if there is an inversion at a higher altitude, due
 294 to the existence of the urban heat island, the surface layer is often weakly unstable. The stable
 295 stratification situation is rare (Li et al., 2007). Therefore, aerosol fluxes in Beijing are calculated
 296 using Eq. (12) based on the assumption of free convection.

297 Based on the discussion above, the LAS technique is capable to determine the magnitude of
 298 the flux but not the sign. In general, the aerosols are very heterogeneous in space and the measured
 299 fluxes show typically large variation in magnitude including the sign. Over the polluted areas, which
 300 behave as the source, the emissions presumable overwhelmingly exceed the deposition sinks
 301 (Ripamonti et al., 2013). Therefore, a rough quantification of the deposition sink would allow
 302 concluding that the sink term is negligible and the flux quantified by LAS can be assumed to
 303 represent the upward fluxes.

304 2.2 Calculation of the friction velocity and surface-layer characteristic temperature

305 To calculate the aerosol vertical turbulent flux, according to Eq. (10), the values of the friction
 306 velocity u^* and the characteristic temperature T^* are required. These can be obtained via wind speed
 307 and temperature profile data. From the near-surface similarity theory, the temperature and wind
 308 speed data measured at two heights of z_1 and z_2 can be used in the expressions of the friction velocity
 309 u^* and the characteristic temperature T^* (Stull, 1988) as follows:

$$310 \quad u_* = \frac{\kappa[U(z_2) - U(z_1)]}{\ln \frac{z_2}{z_1} - \Psi_U(\xi_2) + \Psi_U(\xi_1)} \quad (13)$$

$$311 \quad T_* = \frac{\kappa[T(z_2) - T(z_1)]}{0.74[\ln \frac{z_2}{z_1} - \Psi_T(\xi_2) + \Psi_T(\xi_1)]} \quad (14)$$

312 where $U(z_1)$ and $U(z_2)$ are the measured velocities at heights z_1 and z_2 , respectively, $T(z_1)$ and $T(z_2)$
 313 are the measured temperatures at heights z_1 and z_2 , respectively, ξ_1 and ξ_2 are the stabilities at heights
 314 z_1 and z_2 , respectively, and Ψ_U and Ψ_T are the correction terms for the velocity and temperature
 315 profiles under the condition of stability L . Under unstable conditions (Stull, 1988), we have the
 316 following:

$$317 \quad \Psi_U(\xi) = \ln\left[\left(\frac{1+x^2}{2}\right)\left(\frac{1+x}{2}\right)^2\right] - 2 \arctan(x) + \frac{\pi}{2}, \quad x = (1-15\xi)^{1/4} \quad (15)$$

$$318 \quad \Psi_T(\xi) = \ln\left[\left(\frac{1+y}{2}\right)^2\right], \quad y = (1-9\xi)^{1/2} \quad (16)$$

319 Under stable conditions (Cheng and Brutsaert, 2005), we have the following:

$$320 \quad \Psi_U(\xi) = -a \ln[\xi + (1 + \xi^b)^{1/b}], \quad a=6.1, \quad b=2.5. \quad (17)$$

$$321 \quad \Psi_T(\xi) = -c \ln[\xi + (1 + \xi^d)^{1/d}], \quad c=5.3, \quad d=1.1. \quad (18)$$

322 Based on Eqs. (13)-(18), the friction velocity u^* and characteristic temperature T^* can be
 323 determined.

324 **3 Measurements and data processing**

325 **3.1 Introduction of Experiments**

326 Observations were collected at two locations (two rectangles in Fig. 1a) from December 2016
 327 to March 2017: a rural site in Gucheng (GC site), Hebei Province and an urban site at the Chinese
 328 Academy of Meteorological Sciences (CAMS site) in Beijing. The distance between the two
 329 locations is approximately 100 km. According to the theoretical methods defined in the preceding
 330 section, to estimate the aerosol turbulent flux, the ratio of the aerosol mass to the imaginary part of
 331 the AERI, the ratio of the temperature to the real part of the AERI, the real and imaginary parts of
 332 the atmospheric equivalent refractive index structure parameter (AERISP, $C_{n,Re}^2$ and $C_{n,Im}^2$), the
 333 friction speed, and the characteristic temperature must all be obtained. If the free convection
 334 condition is satisfied, fewer parameters are required, including the real and imaginary parts of the
 335 AERISP, the ratio of the aerosol mass to the imaginary part of the AERI, the ratio of the temperature
 336 to the real part of the AERI, and the atmospheric temperature.

337 Two sets of LASs developed by our research group were installed at the top of the building of
 338 the Chinese Academy of Meteorological Sciences (point A in Fig. 1b) and at the top of a two-story
 339 building in the farm of the Central Meteorological Bureau of Gucheng Town, Baoding City (point
 340 D in Fig. 1c). The light intensity sampling frequency of the receiving end was 500 Hz, and a file
 341 was recorded every 20 minutes. Then, the real and imaginary parts of the AERISP were calculated.
 342 In the CAMS site, the transmitter end of the LAS was placed on the roof of a building on the east
 343 side of the Chinese Academy of Meteorological Sciences, and the receiver end was placed at the top
 344 of the Chinese Academy of Meteorological Sciences. The propagation path was along an east-west
 345 direction. The distance between the two ends was 550 meters as shown in Fig. 1d. The light beam
 346 passed over urban buildings, residential areas and urban roads. The beam height was 43 meters. The
 347 average height of the building below the beam was 24 meters; thus, the zero-displacement was 18
 348 meters ($24 * 0.67 = 18$) (Leclerc and Foken, 2014), and the effective height of the beam was 25

349 meters. At the Beijing observation point, the conventional meteorological parameters are measured
350 on the same roof, 20 meters away from the receiving end and in the northwest direction of the
351 receiving end. The measurement heights were 1.5 m and 10 m above the roof for air temperature
352 and wind speed. To calculate the aerosol flux, it is necessary to obtain the ratio of the aerosol mass
353 to the imaginary part of AERI and to measure the aerosol mass concentration and visibility. In
354 Haidian District, there is a site to measure the visibility of the near-surface layer (point B in Fig.
355 1b), and the PM₁₀ mass concentration measurements were collected at Guanyuan Station (see point
356 C in Fig. 1B). The sampling interval for the visibility and PM₁₀ mass concentration measurements
357 was 1 h. The measurement height of points B and C in Fig. 1b was approximately 20 metres. The
358 ratio of the aerosol mass PM₁₀ to the imaginary part of the AERI was calculated based on the data.
359 The measurements were collected at the CAMS site from 15 January 2017 to 20 March 2017.

360 In the GC site (point D in Fig. 1c, namely, the LAS position) of Gucheng, Baoding, Hebei, the
361 transmitter of the LAS was placed on the roof of a two-story building with a height of 8 m, and the
362 receiving end was located in a room in a three-story building on the west side of National Highway
363 107 at the same height as the transmitting end. The distance between the transmitting end and the
364 receiving end was 1670 metres. The terrain between the transmitting end and the receiving end was
365 flat, with farmland, a national road and sporadic trees below the beam, as seen in Fig. 1e. Near the
366 light beam, there was a 30-meter-high meteorological observation tower, in which the temperature,
367 relative humidity (RH), and wind speed were measured at five levels (1 m, 3 m, 8 m, 18 m, and 28
368 m). The friction speed and characteristic temperature were calculated according to the temperature
369 wind speed profile. Visibility observations were made in Xushui District near the LAS position (see
370 point E in Fig. 1c). The PM₁₀ mass concentration was measured in Beishi District (see point F in
371 Fig. 1c). From Fig. 1c, the three observation points (points D, E and F in Fig. 1c) formed a nearly
372 straight line and were distributed in a northeast-southwest direction. During the experimental
373 observation period, a northeast-southwest wind prevailed; thus, the Xushui District visibility data
374 and Beishi District PM₁₀ data can approximate the situation of the scintillometer position. The
375 measurements were collected at the GC site from 17 November 2016 to 30 March 2017.

376 **3.2 Data quality control**

377 There are two types of variables, namely mean variables and fluctuation variables. Mean
378 variables include temperature, wind speed, wind direction, PM₁₀, and visibility for averages of 30
379 minutes or 60 minutes. Data quality control for the mean variables was conducted by comparing the
380 measured data at different heights or at different stations. Same variables between different heights
381 and different locations having the same trend are considered high quality. All the measured mean
382 data were determined to be adequate. Fluctuation variables include the high-frequency intensity
383 fluctuation data measured by the LAS, the real and imaginary parts of the AERISP, and the
384 calculated aerosol flux. Quality control mainly consists of the elimination of spike and
385 supplementing missing data.

386 Peaks in the light intensity fluctuation data appear because the received signal quickly increases
387 when the light signal is blocked, such as due to birds along the transmission path. The data
388 processing program automatically determines this situation. When this happens, the current 20-
389 minute period is rejected. For the real and imaginary parts of the AERISP and the aerosol flux data,
390 (a) 3 times the standard deviation (SD) of the anomaly and (b) 3 times the SD of the difference

391 between adjacent moments (AMD) were determined. A trend of two-hour averages, namely, 6-point
392 moving averages, is first obtained. Then, the difference between the measured value and the trend
393 at each moment was calculated, and the mean and SD of the difference were also calculated. The
394 data with differences from the trend exceeding 3 times the SD were considered as spikes. The
395 method for judging 3 times the SD of the AMD was first to calculate the AMD and then calculate
396 the mean and SD of the AMDs. Any data whose AMD deviated from the mean of the AMD by more
397 than 3 times the SD of the AMD was considered an error. Less than 5% of the data were found to
398 contain spikes or errors.

399 The data determined to be errors were supplemented with the average of the nearby
400 observations. Of course, if data were missing over a long period, the missing gap could not be filled.
401 For this situation, further gap-filling was not considered.

402 Other errors exist in the measurements using a LAS due to specific reasons (Moene et al., 2009);
403 for example, the impact of the deviation of the shape of spectrum from von Karman's scheme and
404 the intermittent variations in the characteristics of that spectrum on the LAS signal were not
405 considered in this study.

406 **4 Results**

407 First, the visibility and PM₁₀ aerosol mass concentration results at the CAMS site and the GC
408 site are given and compared. Then, the characteristics of aerosol transport in typical weather
409 conditions at the CAMS site and the GC site are discussed. Finally, the aerosol flux characteristics
410 during the HPEs are analyzed.

411 **4.1 Relationship between n_{im} and PM₁₀**

412 To obtain the ratio of the atmospheric aerosol mass concentration to the imaginary part of the
413 AERI (n_{im}) R_{MN} , PM₁₀ and visibility were measured.

414 The maximum PM₁₀ concentration in the Baoding area appeared at 1:00 on January 28, 2017
415 (up to 1071 $\mu\text{g m}^{-3}$), and the maximum PM₁₀ concentration in the Beijing area appeared at 2:00 on
416 January 28, 2017 (up to 917 $\mu\text{g m}^{-3}$). This heavy pollution event swept through Beijing and the
417 surrounding areas, reaching a maximum at almost the same time. The visibility at the corresponding
418 time was less than 500 meters. The imaginary part of the AERI can be calculated from the visibility
419 according to Eq. (7). Fig. 2a shows a relationship plot of the imaginary parts of the AERI and PM₁₀
420 data measured in the Beijing area; there is a strong correlation between the AERI and aerosol particle
421 mass concentration, with a linear correlation coefficient of 0.96. The fitted line in Fig. 2a has a slope
422 of 3845 kg m^{-3} . Therefore, R_{MN} was taken as 3845 kg m^{-3} for the Beijing area to estimate the aerosol
423 vertical turbulent flux. Similarly, Fig. 2b shows the results for the Baoding area, and R_{MN} was set to
424 3711 kg m^{-3} for the Baoding area to estimate the aerosol vertical turbulent flux. The two ratio
425 coefficients are relatively close. Figs. 2a and 2b also show that in the case of light pollution, Beijing's
426 R_{MN} is slightly larger.

427 Furthermore, Figs. 2a and 2b show that although there is a significant scattering between PM₁₀
428 and n_{im} that may be attributed to a significant separation between the two measurement locations
429 for visibility and PM₁₀, there is a strong linear correlation between the imaginary part of the AERI
430 and PM₁₀. The imaginary part of the AERI has a slightly stronger relationship with the PM₁₀ data
431 obtained in the Baoding area than in the Beijing area.

432 R_{MN} should be obtained by simultaneously measuring Ma and the imaginary part of the AERI
433 at the same location with the LAS, so that real-time R_{MN} can be obtained. For GC site and CAMS
434 site, measuring positions of PM_{10} and visibility are a little far from LAS measurement. So a constant
435 ratio R_{MN} is more representative than a simultaneous value.

436 The following provides the results of the aerosol turbulent flux under typical weather
437 conditions in Beijing and Baoding for the period from 10 March 2017 to 17 March 2017.

438 4.2 Characteristics of aerosol flux in the Beijing region

439 To analyze the aerosol turbulent flux characteristics, we present the time series of the
440 conventional meteorological parameters. The time series of temperature, RH, wind speed, wind
441 direction, PM_{10} , $C_{n,Re}^2$, $C_{n,Im}^2$ and aerosol flux are shown in Figs. 3a-3h, respectively. The
442 temperature has a distinct diurnal variation, indicating that this period had primarily sunny weather.
443 The RH from 10 March 2017 to 17 March 2017, was less than 60%, and the RH for most of the
444 period was less than 30%. The wind speed was low; only during the period from March 11 to March
445 14 was the wind moderately strong. At 6:00 on March 12, the maximum wind speed was 4.2 m s^{-1} .
446 At that time, the wind direction has diurnal variation, which is related to the sea-land breeze, valley
447 wind and urban heat island circulation which may exist under the control of weak weather system(Li
448 et al., 2019). Moreover, two light pollution events occurred (MEP, 2012) on March 11 and March
449 16, with PM_{10} concentrations approaching $200 \mu\text{g m}^{-3}$. From the data of $C_{n,Re}^2$ and $C_{n,Im}^2$ in Figs. 3f
450 and 3g, the real part of the AERISP $C_{n,Re}^2$ has obvious diurnal variations, i.e., smaller in the morning
451 and at night and larger at noon. The imaginary part of the AERISP $C_{n,Im}^2$ had no distinct diurnal
452 variation. According to Fig. 3g, there are some peak values, i.e., some sudden increases and
453 decreases, which may be related to sudden changes in wind direction, as shown in Fig. 3d.

454 The LAS at the CAMS site was located in the roughness layer, so the local similarity theory
455 should in principle applied to flux calculation. Because there was no measurement of wind speed
456 and temperature profiles near the LAS measurement location, the friction velocity and characteristic
457 temperature could not be calculated. We (Yuan et al, 2015) conducted a test experiment for aerosol
458 vertical flux in Hefei, China, using free convection assumptions and local similarity theories to
459 calculate aerosol fluxes. Comparison of the calculation results of the two methods shows that very
460 unstable condition accounts for about 62 % of the time, and the relative difference is about 5%.
461 Under weak unstable and stable condition, the relative error is about 15%.

462 From the aerosol flux time series given in Fig. 3h, the aerosol flux is large at noon and small
463 in the morning and at night, which is mainly because of the strong convection at noon. However,
464 large aerosol fluxes also occurred on the nights of March 11 and March 12, which were related to
465 high wind speeds. The mean aerosol flux measured at this observation point during this period was
466 $0.0039 \text{ mg m}^{-2} \text{ s}^{-1}$.

467 4.3 Characteristics of aerosol flux at the GC site

468 Similarly, Figs. 4a-4d provide the time series of temperature, RH, wind speed and wind
469 direction at 3 meters and 18 meters for the GC site, and Figs. 4e-4h show the PM_{10} , $C_{n,Re}^2$, $C_{n,Im}^2$
470 and aerosol flux curves over time. According to Fig. 4a, the temperatures at both heights show
471 distinct diurnal variations. The daytime is characterized by unstable stratification, and at night,

472 stable stratification prevails. Moreover, in the morning and evening, there is a transition period
473 between stable and unstable stratification. Here, u^* , T^* and MO length L were calculated from the
474 wind speed and temperature measured at 3 m and 18 m on a meteorological tower. Fig. 4b shows a
475 plot of the two levels of RH over time, again with apparent diurnal variations. The RH of the GC
476 site was lower at the CAMS site. Figs. 4c and 4d provide the time series of wind speeds and wind
477 directions at two levels. At 6:00 on March 12, the wind speed was relatively high, and the maximum
478 at 18 meters was 6.5 m s^{-1} . At the same time, the maximum wind speed was reached in the Beijing
479 area, although the speed was lower in Beijing. The overall trend of wind direction at the GC site
480 was more consistent with the results of the CAMS site.

481 Figure 4e shows the PM_{10} trend of over time. There were two light pollution events on March
482 11 and March 16. The overall trend is the same as in Fig. 3(e). Figs. 4f and 4g show the time series
483 of the imaginary and real parts of the AERISP for the GC site. The real part of the AERISP is large
484 at noon, and the optical turbulence is strong. The real part of the AERISP is small during the morning
485 and evening, and the corresponding turbulence is weak. The imaginary part of the AERISP given in
486 Fig. 4g does not show an apparent diurnal variation, and there may be some sharp peaks.

487 Figure 4h shows the aerosol mass vertical flux changes over time. The aerosol flux has a
488 significant diurnal variation characteristic associated with turbulent transport near the surface. The
489 mean aerosol flux measured at the GC site during this period was $0.0016 \text{ mg m}^{-2} \text{ s}^{-1}$. This value is
490 much smaller than the results for the CAMS site. Human activities contribute to increased water
491 vapor releases in urban areas compared to rural areas, as observed by Dou et al (2014), and
492 especially for the night-time SBL in winter. During our observation period, the RH of the city was
493 lower than the rural area. However, human activities cause more aerosol particles in urban areas
494 than in rural areas.

495 4.4 Aerosol flux during HPEs

496 In the winter of 2016, there were several HPEs. A heavy pollution event began on 1 December
497 2016 and ended on 10 January 2017. Relevant observational experiments were performed in the
498 Beijing and Baoding areas, including observations of meteorological parameters and aerosol
499 parameters, to understand the causes of the heavy pollution.

500 According to the definition of HPEs and classification, there were 7 TS stages in the 2016
501 winter heavy pollution event, and the AS stage appeared immediately after 4 TS stages. These
502 included 00:00 on December 1 to 03:20 on December 4, 18:40 on December 15 to 00:00 on
503 December 22, 00:00 on December 29 to January 2, and 00:00 and 8:40 on January 2 to 00:00 on
504 January 5.

505 During this period, we used a LAS to conduct an observational study of the vertical aerosol
506 flux in the GC site, which was from 00:00 on December 1, 2016, to 00:00 on December 22, 2016.
507 No corresponding observations were made at the Beijing site during this period. Here, we first
508 discuss the observation results of the GC site, Baoding City, as shown in Fig. 5. Fig. 5a shows the
509 time series of the aerosol vertical turbulent flux. Figs. 5b-5g indicate the time series for the real and
510 imaginary parts of the AERISP, the temperature and RH at 18 meters, and the wind speed and
511 direction. Purple curves indicate the TS stages, red curves show the AS stages, and grey curves
512 show the RS stages.

513 According to Fig. 5a, in the TS stages and the RS stages, the aerosol flux exhibited diurnal

514 variations, while the AS stage did not show a diurnal variation. There were some peaks in the TS
515 stage. The average aerosol flux of the TS stages was $0.00065 \text{ mg m}^{-2} \text{ s}^{-1}$, the average value of the
516 AS stages was $0.00025 \text{ mg m}^{-2} \text{ s}^{-1}$, and the average value of the RS stages was $0.00063 \text{ mg m}^{-2} \text{ s}^{-1}$.
517 The aerosol turbulent fluxes in the TS and RS stages were similar, while the aerosol turbulent flux
518 in the AS stage was much smaller than the TS and RS stages.

519 According to Fig. 5b-5c, the imaginary structure parameters and the real structure parameters
520 of the refractive index in the TS and RS stages exhibited diurnal variations, while the AS stage did
521 not exhibit a diurnal variation. Fig. 5d shows that except for the second AS event (22:00 on 19
522 December 2016 to 00:00, 22 December 2016), the temperature showed a diurnal variation. During
523 the AS stage, the RH (see Fig. 5e) was close to 100%, while the RH during the TS and RS stages
524 were lower. Moreover, Fig. 5f shows that during this time, the wind speed was relatively weak,
525 although the wind speed was slightly stronger on December 5. As shown in Fig. 5g, during the TS
526 and AS stages, southerly winds prevailed, while during the RS period, northerly winds prevailed.
527 The high wind speed and convection in the TS and RS stages contributed to the upward transport of
528 aerosol particles, whereas the low wind speed and stable stratification in the AS stage were not
529 conducive to the upward transport of aerosol particles.

530 During the heavy pollution period from 1 December 2016 to 10 January 2017, we did not
531 conduct surface aerosol flux observations at the CAMS site. From January 25 to January 31, the
532 pollution in the Beijing area also reached the level of heavy pollution. During this HPE, a
533 measurement of surface aerosol fluxes at the CAMS site was conducted. Figure 6 shows the results
534 of the meteorological and pollutant observations for six days from 00:00 on January 25, 2017 to
535 00:00 on January 31, 2017. According to Fig. 6, northerly winds prevailed after noon on January
536 26, when the concentration of PM_{10} dropped rapidly from $254 \mu\text{g m}^{-3}$ at 12:00 to $5 \mu\text{g m}^{-3}$ at 15:00.
537 During the period 12:00-24:00 on January 26, the average wind speed was 2.6 ms^{-1} . On January 27,
538 southerly winds prevailed, the average wind speed was only 0.8 ms^{-1} , and the aerosol concentration
539 (PM_{10}) increased slowly; the increase began at 6:30 before growing rapidly at 17:50, reaching more
540 than $300 \mu\text{g m}^{-3}$ at 23:00 and $917 \mu\text{g m}^{-3}$ at 2:00 am on January 28, which was the maximum aerosol
541 concentration over the 6 day period. Then, the aerosol concentration decreased gradually. The
542 average wind speed on January 27 was 0.6 ms^{-1} , southerly winds prevailed, and the mean PM_{10}
543 concentration was $440 \mu\text{g m}^{-3}$, which constitutes a severe pollution level. The average PM_{10}
544 concentration during the period from 00:00 on January 25 to 00:00 on January 31 was $170 \mu\text{g m}^{-3}$.

545 According to the previous characteristics for the TS and AS stages, a period of southerly winds
546 can be determined as the TS stage. Thus, January 27 can be designated as the TS stage, January 28
547 can be determined as the AS stage, and January 29 can be determined as the RS stage. During
548 Beijing's heavy pollution event in January 2017 (20170125-20170131), the mean aerosol vertical
549 flux in the TS stage was $0.0024 \text{ mg m}^{-2} \text{ s}^{-1}$, the average value during the AS stage was 0.00087 mg
550 $\text{m}^{-2} \text{ s}^{-1}$ and the RS stage was $0.0049 \text{ mg m}^{-2} \text{ s}^{-1}$. The overall average value was $0.0032 \text{ mg m}^{-2} \text{ s}^{-1}$.

551 Even during heavy pollution events, the RH in Beijing was lower than in the outer suburbs.
552 According to Fig. 6e, the RH exceeded 60% in the period from 3:00 to 6:00 on January 26, where
553 the maximum value was 63%, and the RH was less than 60% in the remaining periods. In urban
554 areas, when the RH is low, heavy pollution incidents can occur. In Beijing, during the AS stage, the
555 vertical flux of aerosol was less than during the TS and RS stages.

556 **5 Discussions and conclusions**

557 During the winter of 2016 and the spring of 2017, HPEs frequently occurred in the BTH area.
558 This study investigated the aerosol vertical mass flux and compared its magnitude during different
559 stages of HPEs, including RSs, TSs, and ASs, in two representative urban and rural sites, including
560 the CAMS site in Beijing and the GC site in Hebei Province. Based on the light propagation theory
561 and surface-layer similarity theory, the aerosol vertical mass flux was obtained by combining LAS
562 observations, surface $PM_{2.5}$ and PM_{10} mass concentrations, and meteorological observations,
563 including air temperature and RH. We found that under favorable meteorological conditions for
564 pollution dispersion, i.e., from 10 March 2017 to 17 March 2017, the vertical aerosol mass flux
565 exhibited striking diurnal variations, with the mass fluxes reaching peak values at noon and lowering
566 in the morning and evening. During the HPEs from 25 January 2017 to 31 January 2017 in Beijing,
567 the vertical aerosol mass flux varied substantially during the different stages. Specifically, the mean
568 mass flux decreased by 51% from $0.0049 \text{ mg m}^{-2}\text{s}^{-1}$ in the RSs to $0.0024 \text{ mg m}^{-2}\text{s}^{-1}$ in the TSs, which
569 was partly due to the wind speed reduction from strong northerly winds in the RSs to southerly
570 winds in the TSs. During the ASs, the mean mass flux decreased further to $0.00087 \text{ mg m}^{-2}\text{s}^{-1}$, which
571 accounted for approximately 1/3 of the flux during the TSs. The weakened mass flux would further
572 facilitate aerosol accumulation. During the HPE from December 01, 2016, to December 22, 2016,
573 in Gucheng, the mean mass flux was similar in the RSs and TSs, ranging from $0.00063 \text{ mg m}^{-2}\text{s}^{-1}$ to
574 $0.00065 \text{ mg m}^{-2}\text{s}^{-1}$. This is partly because Gucheng was less affected by strong northerly winds than
575 Beijing. Thus, the wind speed varied slightly from the RSs to TSs. However, the mass flux decreased
576 substantially to $0.00025 \text{ mg m}^{-2}\text{s}^{-1}$ in the ASs, which was merely 1/3 of the mean flux in the TSs.

577 Based on our measurement results, it can be seen that from the TS to the AS, the aerosol vertical
578 turbulent flux decreased, but the aerosol particle concentration with surface layer increased. It is
579 inferred that in addition to the contribution of regional transport from upwind areas during the TS,
580 suppression of vertical turbulence mixing confining aerosols to a shallow boundary layer increased
581 accumulation.

582 In this study, the aerosol emission flux was also estimated in these two rural and urban sites.
583 Generally, compared with the emissions in spring, we found that in winter, the near-ground
584 emissions were weaker in suburban areas and were similar in urban areas. In suburban areas,
585 although the aerosol concentrations were relatively high (Shen et al., 2018), the upward emitted
586 aerosol flux was smaller than in urban areas. During the ASs of the HPEs, the aerosol emission flux
587 from near-ground emission sources was weaker than for the RSs and TSs at both the CAMS and
588 GC sites, which indicates that surface pollutant emissions are not the major cause of explosive $PM_{2.5}$
589 growth. During the ASs with weak solar radiation, the factors most associated with aerosol
590 concentration changes were horizontal transport and BL height variations, which might be the
591 leading causes of increased $PM_{2.5}$. This is in line with previous studies that the main reason for the
592 explosive growth of aerosol concentration during AS is attributed to the horizontal transport during
593 TS. The TS will definitely appear before CS. The south or southwest wind will always appear in the
594 TS, and the concentration of PM_{10} in Baoding is higher than the mass of PM_{10} in Beijing, which is
595 generally maintained for one to two days. Except for the southerly or southwesterly winds for one
596 to two days, there will be no CS in Beijing. Even if it is a southerly or southwesterly wind, if the
597 wind speed is too small ($<1 \text{ ms}^{-1}$), AS will not appear. Only the southerly or southwesterly wind with
598 a wind speed greater than a specific value ($>1.5 \text{ m s}^{-1}$), and the concentration of PM_{10} in the area to

599 the south of Beijing is higher than that in Beijing, and then there will be CS after a small wind
600 (Zhong et al., 2018c; Zhong et al., 2018b; Zhang et al., 2018).

601 Compared to the results (Yuan et al. 2016) from Hefei, China, a small and medium-sized
602 provincial capital city in East China, the measured aerosol mass-fluxes in Beijing are almost at the
603 same amount. A series of measures and actions have been made for emission reduction in Beijing,
604 and the main emission is from vehicles. The difference in aerosol mass flux may be small.

605 Due to the lack of necessary experimental conditions, such as meteorological towers and EC
606 systems, current experimental results cannot be compared with EC methods. According to the
607 literature data, the two methods have been compared indirectly, and the estimated aerosol flux under
608 different measurement conditions is consistent in magnitude (Yuan et al., 2016). However, a direct
609 comparison of the two methods is in development.

610 Compared with the EC method, the aerosol flux has high spatial representativeness based on
611 the principle of light propagation, and there is no need to install a tall tower. However, the estimation
612 of aerosol fluxes using the LAS method still has theoretical and practical deficiencies. At present,
613 the LAS method for the aerosol flux regards the aerosol particles as ordinary scalar molecules. At
614 the same time, based on the assumption of the equivalent medium, the imaginary part of the AERI
615 is taken for granted as proportional to the aerosol mass concentration. This is often not the case. The
616 actual turbulence spectrum shape may deviate from von Karman spectrum, and turbulence
617 intermittent and scintillation saturation can also occur (Moene et al., 2009). The applicability of the
618 near-surface layer similarity theory to the aerosol particle motion under stable layer conditions also
619 has many problems. The formation of new particles and changes in aerosol particle size distribution
620 also affect the scintillation in light propagation. There are also practical problems such as untimely
621 maintenance, rainfall and low visibility, and platform vibrations required for observation. All these
622 problems will cause errors in final estimates, so more theoretical and experimental research is
623 needed.

624 **Data availability.** Requests for data that support the findings of this study can be sent to
625 rmyuan@ustc.edu.cn.

626 **Competing interests.** The authors declare that they have no conflict of interest.

627 **Author contributions.** Renmin Yuan and Xiaoye Zhang designed experiments and wrote the manuscript;
628 Renmin Yuan, Hao Liu, Yu Gui, Bohao Shao, Yaqiang Wang, Junting Zhong and Xaioping Tao
629 carried out experiments; Renmin Yuan analyzed experimental results. Yubin Li and Zhiqiu Gao
630 designed experiments and discussed the results.

631 **Acknowledgements.** This study was supported by the National Key Research and Development Program
632 under grant no. 2016YFC0203306 and the National Natural Science Foundation of China
633 (41775014, 51677175). We also thank two anonymous reviewers for their constructive and helpful
634 comments.

635 **References**

- 636 Ahlm, L., Krejci, R., Nilsson, E. D., Martensson, E. M., Vogt, M., and Artaxo, P.: Emission and dry deposition of
637 accumulation mode particles in the Amazon Basin, *Atmospheric Chemistry And Physics*, 10, 10237-10253,
638 10.5194/acp-10-10237-2010, 2010a.
- 639 Ahlm, L., Nilsson, E. D., Krejci, R., Martensson, E. M., Vogt, M., and Artaxo, P.: A comparison of dry and wet
640 season aerosol number fluxes over the Amazon rain forest, *Atmospheric Chemistry and Physics*, 10, 3063-3079,
641 10.5194/acp-10-3063-2010, 2010b.

642 Akagi, S. K., Yokelson, R. J., Wiedinmyer, C., Alvarado, M. J., Reid, J. S., Karl, T., Crounse, J. D., and Wennberg,
643 P. O.: Emission factors for open and domestic biomass burning for use in atmospheric models, *Atmospheric*
644 *Chemistry And Physics*, 11, 4039-4072, 10.5194/acp-11-4039-2011, 2011.

645 Bond, T. C., Streets, D. G., Yarber, K. F., Nelson, S. M., Woo, J. H., and Klimont, Z.: A technology-based global
646 inventory of black and organic carbon emissions from combustion, *Journal Of Geophysical Research-*
647 *Atmospheres*, 109, 10.1029/2003jd003697, 2004.

648 Brion, J., Chakir, A., Charbonnier, J., Daumont, D., Parisse, C., and Malicet, J.: Absorption spectra measurements
649 for the ozone molecule in the 350-830 nm region, *J. Atmos. Chem.*, 30, 291-299, 10.1023/a:1006036924364,
650 1998.

651 Brooks, I. M., Yelland, M. J., Upstill-Goddard, R. C., Nightingale, P. D., Archer, S., d'Asaro, E., Beale, R., Beatty,
652 C., Blomquist, B., Bloom, A. A., Brooks, B. J., Cludera, J., Coles, D., Dacey, J., DeGrandpre, M., Dixon, J.,
653 Drennan, W. M., Gabriele, J., Goldson, L., Hardman-Mountford, N., Hill, M. K., Horn, M., Hsueh, P.-C.,
654 Huebert, B., de Leeuw, G., Leighton, T. G., Liddicoat, M., Lingard, J. J. N., McNeil, C., McQuaid, J. B., Moat,
655 B. I., Moore, G., Neill, C., Norris, S. J., O'Doherty, S., Pascal, R. W., Prytherch, J., Rebozo, M., Sahlee, E.,
656 Salter, M., Schuster, U., Skjelvan, I., Slagter, H., Smith, M. H., Smith, P. D., Srokosz, M., Stephens, J. A.,
657 Taylor, P. K., Telszewski, M., Walsh, R., Ward, B., Woolf, D. K., Young, D., and Zemmelen, H.: Physical
658 exchanges at the air-sea interface uk-solas field measurements, *Bulletin of the American Meteorological Society*,
659 90, 629-+, 10.1175/2008bams2578.1, 2009.

660 Buzorius, G., Rannik, U., Makela, J. M., Vesala, T., and Kulmala, M.: Vertical aerosol particle fluxes measured by
661 eddy covariance technique using condensational particle counter, *Journal of Aerosol Science*, 29, 157-171,
662 10.1016/s0021-8502(97)00458-8, 1998.

663 Cao, J., Xu, H., Xu, Q., Chen, B., and Kan, H.: Fine Particulate Matter Constituents and Cardiopulmonary Mortality
664 in a Heavily Polluted Chinese City, *Environmental Health Perspectives*, 120, 373-378, 10.1289/ehp.1103671,
665 2012.

666 Ceburnis, D., Rinaldi, M., Ovadnevaite, J., Martucci, G., Giulianelli, L., and O'Dowd, C. D.: Marine submicron
667 aerosol gradients, sources and sinks, *Atmospheric Chemistry and Physics*, 16, 12425-12439, 10.5194/acp-16-
668 12425-2016, 2016.

669 Chen, Y., Tian, C., Feng, Y., Zhi, G., Li, J., and Zhang, G.: Measurements of emission factors of PM_{2.5}, OC, EC,
670 and BC for household stoves of coal combustion in China, *Atmospheric Environment*, 109, 190-196,
671 10.1016/j.atmosenv.2015.03.023, 2015.

672 Cheng, Y. G., and Brutsaert, W.: Flux-profile relationships for wind speed and temperature in the stable atmospheric
673 boundary layer, *Boundary-Layer Meteorology*, 114, 519-538, 10.1007/s10546-004-1425-4, 2005.

674 DeBruin, H. A. R., vandenHurk, B., and Kohsiek, W.: The scintillation method tested over a dry vineyard area,
675 *Boundary-Layer Meteorology*, 76, 25-40, 1995.

676 Dou, J., Wang, Y., and Miao, S.: Fine Spatial and Temporal Characteristics of Humidity and Wind in Beijing Urban
677 Area, *Journal of Applied Meteorological Science*, 25, 559-569, 2014.

678 Dubovik, O., Holben, B., Eck, T. F., Smirnov, A., Kaufman, Y. J., King, M. D., Tanre, D., and Slutsker, I.: Variability
679 of absorption and optical properties of key aerosol types observed in worldwide locations, *J. Atmos. Sci.*, 59,
680 590-608, 10.1175/1520-0469(2002)059<0590:voaaop>2.0.co;2, 2002.

681 Elbert, W., Taylor, P. E., Andreae, M. O., and Poeschl, U.: Contribution of fungi to primary biogenic aerosols in the
682 atmosphere: wet and dry discharged spores, carbohydrates, and inorganic ions, *Atmospheric Chemistry and*
683 *Physics*, 7, 4569-4588, 10.5194/acp-7-4569-2007, 2007.

684 EPD, E. P. D.: Technical regulation on ambient air quality index (on trial), Beijing, 12 pp., 2012.

685 Evans, J. G., and De Bruin, H. A. R.: The Effective Height of a Two-Wavelength Scintillometer System, *Bound-Lay.*

686 Meteorol., 141, 165-177, 10.1007/s10546-011-9634-0, 2011.

687 Farmer, D. K., Kimmel, J. R., Phillips, G., Docherty, K. S., Worsnop, D. R., Sueper, D., Nemitz, E., and Jimenez, J.
688 L.: Eddy covariance measurements with high-resolution time-of-flight aerosol mass spectrometry: a new
689 approach to chemically resolved aerosol fluxes, *Atmos. Meas. Tech.*, 4, 1275-1289, 10.5194/amt-4-1275-2011,
690 2011.

691 Gordon, M., Staebler, R. M., Liggio, J., Vlasenko, A., Li, S.-M., and Hayden, K.: Aerosol flux measurements above
692 a mixed forest at Borden, Ontario *Atmos. Chem. Phys.*, 11, 6773-6786, 2011.

693 Graham, B., Guyon, P., Taylor, P. E., Artaxo, P., Maenhaut, W., Glovsky, M. M., Flagan, R. C., and Andreae, M. O.:
694 Organic compounds present in the natural Amazonian aerosol: Characterization by gas chromatography-mass
695 spectrometry, *Journal Of Geophysical Research-Atmospheres*, 108, 10.1029/2003jd003990, 2003.

696 Guo, H., Xu, M., and Hu, Q.: Changes in near-surface wind speed in China: 1969-2005, *International Journal Of*
697 *Climatology*, 31, 349-358, 10.1002/joc.2091, 2011.

698 Guo, S., Hu, M., Zamora, M. L., Peng, J. F., Shang, D. J., Zheng, J., Du, Z. F., Wu, Z., Shao, M., Zeng, L. M., Molina,
699 M. J., and Zhang, R. Y.: Elucidating severe urban haze formation in China, *Proc. Natl. Acad. Sci. U.S.A.*, 111,
700 17373-17378, 10.1073/pnas.1419604111, 2014.

701 Harrison, R. M., Dall'Osto, M., Beddows, D. C. S., Thorpe, A. J., Bloss, W. J., Allan, J. D., Coe, H., Dorsey, J. R.,
702 Gallagher, M., Martin, C., Whitehead, J., Williams, P. I., Jones, R. L., Langridge, J. M., Benton, A. K., Ball, S.
703 M., Langford, B., Hewitt, C. N., Davison, B., Martin, D., Petersson, K. F., Henshaw, S. J., White, I. R.,
704 Shallcross, D. E., Barlow, J. F., Dunbar, T., Davies, F., Nemitz, E., Phillips, G. J., Helfter, C., Di Marco, C. F.,
705 and Smith, S.: Atmospheric chemistry and physics in the atmosphere of a developed megacity (London): an
706 overview of the REPARTEE experiment and its conclusions, *Atmos. Chem. Phys.*, 12, 3065-3114,
707 10.5194/acp-12-3065-2012, 2012, 2012.

708 Hartogensis, O. K., Watts, C. J., Rodriguez, J. C., and De Bruin, H. A. R.: Derivation of an effective height for
709 scintillometers: La Poza experiment in Northwest Mexico, *Journal of Hydrometeorology*, 4, 915-928,
710 10.1175/1525-7541(2003)004<0915:doaehf>2.0.co;2, 2003.

711 He, Y., Gao, Z., Guo, T., Qu, F., Liang, D., Li, D., Shi, J., and Shan, B.: Fine particulate matter associated mortality
712 burden of lung cancer in Hebei Province, China, *Thoracic Cancer*, 9, 820-826, 10.1111/1759-7714.12653, 2018.

713 Hourdin, F., Gueye, M., Diallo, B., Dufresne, J. L., Escribano, J., Menut, L., Marticorena, B., Siour, G., and Guichard,
714 F.: Parameterization of convective transport in the boundary layer and its impact on the representation of the
715 diurnal cycle of wind and dust emissions, *Atmospheric Chemistry and Physics*, 15, 6775-6788, 10.5194/acp-
716 15-6775-2015, 2015.

717 Huang, R.-J., Zhang, Y., Bozzetti, C., Ho, K.-F., Cao, J.-J., Han, Y., Daellenbach, K. R., Slowik, J. G., Platt, S. M.,
718 Canonaco, F., Zotter, P., Wolf, R., Pieber, S. M., Brun, E. A., Crippa, M., Ciarelli, G., Piazzalunga, A.,
719 Schwikowski, M., Abbaszade, G., Schnelle-Kreis, J., Zimmermann, R., An, Z., Szidat, S., Baltensperger, U., El
720 Haddad, I., and Prevot, A. S. H.: High secondary aerosol contribution to particulate pollution during haze events
721 in China, *Nature*, 514, 218-222, 10.1038/nature13774, 2014.

722 Jarvi, L., Rannik, U., Mammarella, I., Sogachev, A., Aalto, P. P., Keronen, P., Siivola, E., Kulmala, M., and Vesala,
723 T.: Annual particle flux observations over a heterogeneous urban area, *Atmos. Chem. Phys.*, 9, 7847-7856,
724 2009.

725 Kaimal, J. C., Izumi, Y., Wyngaard, J. C., and Cote, R.: Spectral characteristics of surface-layer turbulence, *Q. J.*
726 *Roy. Meteor. Soc.*, 98, 563-589, 1972.

727 Karvosenoja, N., Tainio, M., Kupiainen, K., Tuomisto, J. T., Kukkonen, J., and Johansson, M.: Evaluation of the
728 emissions and uncertainties of PM_{2.5} originated from vehicular traffic and domestic wood combustion in
729 Finland, *Boreal Environment Research*, 13, 465-474, 2008.

730 Ketzel, M., Wahlin, P., Berkowicz, R., and Palmgren, F.: Particle and trace gas emission factors under urban driving
731 conditions in Copenhagen based on street and roof-level observations, *Atmospheric Environment*, 37, 2735-
732 2749, 10.1016/s1352-2310(03)00245-0, 2003.

733 Krecl, P., Targino, A. C., Landi, T. P., and Ketzel, M.: Determination of black carbon, PM2.5, particle number and
734 NOx emission factors from roadside measurements and their implications for emission inventory development,
735 *Atmospheric Environment*, 186, 229-240, 10.1016/j.atmosenv.2018.05.042, 2018.

736 Lagouarde, J. P., Irvine, M., Bonnefond, J. M., Grimmond, C. S. B., Long, N., Oke, T. R., Salmond, J. A., and Offerle,
737 B.: Monitoring the sensible heat flux over urban areas using large aperture scintillometry: Case study of
738 Marseille city during the escompte experiment, *Boundary-Layer Meteorology*, 118, 449-476, 10.1007/s10546-
739 005-9001-0, 2006.

740 Leclerc, M. Y., and Foken, T.: *Footprints in Micrometeorology and Ecology*, Springer, Heidelberg, 254 pp., 2014.

741 Lee, X.: *Handbook of Micrometeorology, A Guide for Surface Flux Measurement and Analysis*, edited by: Lee, X.,
742 Kluwer academic publishers, New York, USA, 250 pp., 2004.

743 Lei, H., and Wuebbles, D. J.: Chemical competition in nitrate and sulfate formations and its effect on air quality,
744 *Atmospheric Environment*, 80, 472-477, 10.1016/j.atmosenv.2013.08.036, 2013.

745 Li, J., Sun, J., Zhou, M., Cheng, Z., Li, Q., Cao, X., and Zhang, J.: Observational analyses of dramatic developments
746 of a severe air pollution event in the Beijing area, *Atmospheric Chemistry and Physics*, 18, 3919-3935,
747 10.5194/acp-18-3919-2018, 2018.

748 Li, M., Liu, H., Geng, G., Hong, C., Liu, F., Song, Y., Tong, D., Zheng, B., Cui, H., Man, H., Zhang, Q., and He, K.:
749 Anthropogenic emission inventories in China: a review, *National Science Review*, 4, 834-866,
750 10.1093/nsr/nwx150, 2017.

751 Li, Q.-c., Li, J., Zheng, Z.-f., Wang, Y.-t., and Yu, M.: Influence of mountain valley breeze and sea land breeze in
752 winter on distribution of air pollutants in beijing-tianjin-hebei region, *Environmental Science & Technology*,
753 40, 513-524, 2019.

754 Li, X., Hu, F., and Shu, W.: Study on the characteristics of winter island heat islands in Beijing and the influence
755 factors of strong and weak heat islands, *Journal of the Graduate School of the Chinese Academy of Sciences*,
756 4, 431-438, 2007.

757 Liu, H., Man, H., Cui, H., Wang, Y., Deng, F., Wang, Y., Yang, X., Xiao, Q., Zhang, Q., Ding, Y., and He, K.: An
758 updated emission inventory of vehicular VOCs and IVOCs in China, *Atmospheric Chemistry And Physics*, 17,
759 12709-12724, 10.5194/acp-17-12709-2017, 2017.

760 Lou, S., Liao, H., and Zhu, B.: Impacts of aerosols on surface-layer ozone concentrations in China through
761 heterogeneous reactions and changes in photolysis rates, *Atmos. Environ.*, 85, 123-138,
762 10.1016/j.atmosenv.2013.12.004, 2014.

763 Lu, Z., Zhang, Q., and Streets, D. G.: Sulfur dioxide and primary carbonaceous aerosol emissions in China and India,
764 1996-2010, *Atmospheric Chemistry And Physics*, 11, 9839-9864, 10.5194/acp-11-9839-2011, 2011.

765 Martensson, E. M., Nilsson, E. D., Buzorius, G., and Johansson, C.: Eddy covariance measurements and
766 parameterisation of traffic related particle emissions in an urban environment, *Atmos. Chem. Phys.*, 6, 769-785,
767 2006.

768 Mayol, E., Jimenez, M. A., Herndl, G. J., Duarte, C. M., and Arrieta, J. M.: Resolving the abundance and air-sea
769 fluxes of airborne microorganisms in the North Atlantic Ocean, *Frontiers in Microbiology*, 5,
770 10.3389/fmicb.2014.00557, 2014.

771 MEP, P. R. C.: *Technical regulation on ambient air quality index*, Ministry of Environmental Protection, Beijing, 12
772 pp., 2012.

773 Moene, A. F., Beyrich, F., and Hartogensis, O. K.: Developments in scintillometry, *Bulletin of the American*

774 Meteorological Society, 90, 694-698, 10.1175/2008bams2672.1, 2009.

775 Nebuloni, R.: Empirical relationships between extinction coefficient and visibility in fog, *Appl. Opt.*, 44, 3795-3804,
776 10.1364/ao.44.003795, 2005.

777 Nemitz, E., Dorsey, J. R., Flynn, M. J., Gallagher, M. W., Hensen, A., Erismann, J.-W., Owen, S. M., Ammann, U. D.,
778 and Sutton, M. A.: Aerosol fluxes and particle growth above managed grassland, *Biogeosciences*, 6, 1627-1645,
779 2009.

780 Ripamonti, G., Jarvi, L., Molgaard, B., Hussein, T., Nordbo, A., and Hameri, K.: The effect of local sources on
781 aerosol particle number size distribution, concentrations and fluxes in Helsinki, Finland, *Tellus B.*, 65,
782 10.3402/tellusb.v65i0.19786, 2013.

783 Roden, C. A., Bond, T. C., Conway, S., Benjamin, A., and Pinel, O.: Emission factors and real-time optical properties
784 of particles emitted from traditional wood burning cookstoves, *Environmental Science & Technology*, 40, 6750-
785 6757, 10.1021/es052080i, 2006.

786 Shen, G., Tao, S., Wei, S., Chen, Y., Zhang, Y., Shen, H., Huang, Y., Zhu, D., Yuan, C., Wang, H., Wang, Y., Pei, L.,
787 Liao, Y., Duan, Y., Wang, B., Wang, R., Lv, Y., Li, W., Wang, X., and Zheng, X.: Field Measurement of Emission
788 Factors of PM, EC, OC, PAH, Nitro-, and Oxy- Polycyclic Aromatic Hydrocarbons for Residential Briquette,
789 Coal Cake, and Wood in Rural Shanxi, China, *Environmental Science & Technology*, 47, 2998-3005,
790 10.1021/es304599g, 2013.

791 Shen, X., Sun, J., Zhang, X., Zhang, Y., Wang, Y., Tan, K., Wang, P., Zhang, L., Qi, X., Che, H., Zhang, Z., Zhong,
792 J., Zhao, H., and Ren, S.: Comparison of Submicron Particles at a Rural and an Urban Site in the North China
793 Plain during the December 2016 Heavy Pollution Episodes, *Journal of Meteorological Research*, 32, 26-37,
794 10.1007/s13351-018-7060-7, 2018.

795 Sproson, D. A. J., Brooks, I. M., and Norris, S. J.: The effect of hygroscopicity on eddy covariance estimates of sea-
796 spray aerosol fluxes: a comparison of high-rate and bulk correction methods, *Atmos. Meas. Tech.*, 6, 323-335,
797 2013.

798 Stull, R. B.: *An Introduction to Boundary Layer Meteorology*, Reidel Publishing Co., Dordrecht, 666 pp., 1988.

799 Su, F., Gao, Q., Zhang, Z., Ren, Z.-h., and Yang, X.-x.: Transport pathways of pollutants from outside in
800 atmosphere boundary layer, *Res. Environ. Sci.*, 1, 26-29, 10.13198/j.res.2004.01.28.sufq.005, 2004.

801 Sun, Y., Jiang, Q., Wang, Z., Fu, P., Li, J., Yang, T., and Yin, Y.: Investigation of the sources and evolution processes
802 of severe haze pollution in Beijing in January 2013, *Journal Of Geophysical Research-Atmospheres*, 119, 4380-
803 4398, 10.1002/2014jd021641, 2014.

804 Tatarskii, V. I.: *Wave Propagation in a Turbulent Medium*, McGraw-Hill Book Company Inc., New York, 285 pp.,
805 1961.

806 Vogt, M., Nilsson, E. D., Ahlm, L., Martensson, E. M., and Johansson, C.: Seasonal and diurnal cycles of 0.25-2.5
807 μm aerosol fluxes over urban Stockholm, Sweden, *Tellus B.*, 63, 935-951, 10.1111/j.1600-0889.2011.00551.x,
808 2011a.

809 Vogt, M., Nilsson, E. D., Ahlm, L., Martensson, E. M., and Johansson, C.: The relationship between 0.25-2.5 μm
810 aerosol and CO₂ emissions over a city, *Atmos. Chem. Phys.*, 11, 4851-4859, 10.5194/acp-11-4851-2011, 2011b.

811 Wang, H., Lu, K., Chen, X., Zhu, Q., Wu, Z., Wu, Y., and Sun, K.: Fast particulate nitrate formation via N₂O₅ uptake
812 aloft in winter in Beijing, *Atmospheric Chemistry and Physics*, 18, 10483-10495, 10.5194/acp-18-10483-2018,
813 2018.

814 Wang, Y. H., Liu, Z. R., Zhang, J. K., Hu, B., Ji, D. S., Yu, Y. C., and Wang, Y. S.: Aerosol physicochemical properties
815 and implications for visibility during an intense haze episode during winter in Beijing, *Atmospheric Chemistry
816 And Physics*, 15, 3205-3215, 10.5194/acp-15-3205-2015, 2015.

817 Wang, Z., Li, J., Wang, Z., Yang, W., Tang, X., Ge, B., Yan, P., Zhu, L., Chen, X., Chen, H., Wang, W., Li, J., Liu,

818 B., Wang, X., Wand, W., Zhao, Y., Lu, N., and Su, D.: Modeling study of regional severe hazes over mid-eastern
819 China in January 2013 and its implications on pollution prevention and control, *Science China-Earth Sciences*,
820 57, 3-13, 10.1007/s11430-013-4793-0, 2014.

821 Whitehead, J. D., Gallagher, M. W., Dorsey, J. R., Robinson, N., Gabey, A. M., Coe, H., McFiggans, G., Flynn, M.
822 J., Ryder, J., Nemitz, E., and Davies, F.: Aerosol fluxes and dynamics within and above a tropical rainforest in
823 South-East Asia, *Atmospheric Chemistry and Physics*, 10, 9369-9382, 10.5194/acp-10-9369-2010, 2010.

824 Wu, Q., Wang, Z., Chen, H., Zhou, W., and Wenig, M.: An evaluation of air quality modeling over the Pearl River
825 Delta during November 2006, *Meteorology And Atmospheric Physics*, 116, 113-132, 10.1007/s00703-011-
826 0179-z, 2012.

827 Wyngaard, J. C., Izumi, Y., and Collins, S. A.: Behavior of refractive-index-structure parameter near ground, *J. Opt.*
828 *Soc. Am.*, 61, 1646-1650, 10.1364/josa.61.001646, 1971.

829 Wyngaard, J. C.: *Turbulence in the Atmosphere*, Cambridge University Press, New York, 393 pp., 2010.

830 Yuan, R., Luo, T., Sun, J., Zeng, Z., Ge, C., and Fu, Y.: A new method for measuring the imaginary part of the
831 atmospheric refractive index structure parameter in the urban surface layer, *Atmospheric Chemistry and Physics*,
832 15, 2521-2531, 10.5194/acp-15-2521-2015, 2015.

833 Yuan, R., Luo, T., Sun, J., Liu, H., Fu, Y., and Wang, Z.: A new method for estimating aerosol mass flux in the urban
834 surface layer using LAS technology, *Atmospheric Measurement Techniques*, 9, 1925-1937, 10.5194/amt-9-
835 1925-2016, 2016.

836 Zeweldi, D. A., Gebremichael, M., Wang, J., Sammis, T., Kleissl, J., and Miller, D.: Intercomparison of Sensible
837 Heat Flux from Large Aperture Scintillometer and Eddy Covariance Methods: Field Experiment over a
838 Homogeneous Semi-arid Region, *Bound-Lay. Meteorol.*, 135, 151-159, 10.1007/s10546-009-9460-9, 2010.

839 Zhang, H., and Li, X.: Review of the field measurements and parameterization for dust emission during sand-dust
840 events, *Journal of Meteorological Research*, 28, 903-922, 10.1007/s13351-014-3296-z, 2014.

841 Zhang, Q., Streets, D. G., Carmichael, G. R., He, K. B., Huo, H., Kannari, A., Klimont, Z., Park, I. S., Reddy, S., Fu,
842 J. S., Chen, D., Duan, L., Lei, Y., Wang, L. T., and Yao, Z. L.: Asian emissions in 2006 for the NASA INTEX-
843 B mission, *Atmospheric Chemistry And Physics*, 9, 5131-5153, 10.5194/acp-9-5131-2009, 2009a.

844 Zhang, X., Zhong, J., Wang, J., Wang, Y., and Liu, Y.: The interdecadal worsening of weather conditions affecting
845 aerosol pollution in the Beijing area in relation to climate warming, *Atmospheric Chemistry and Physics*, 18,
846 5991-5999, 10.5194/acp-18-5991-2018, 2018.

847 Zhang, X. Y., Wang, Y. Q., Lin, W. L., Zhang, Y. M., Zhang, X. C., Gong, S., Zhao, P., Yang, Y. Q., Wang, J. Z., Hou,
848 Q., Zhang, X. L., Che, H. Z., Guo, J. P., and Li, Y.: CHANGES OF ATMOSPHERIC COMPOSITION AND
849 OPTICAL PROPERTIES OVER BEIJING 2008 Olympic Monitoring Campaign, *Bulletin Of the American*
850 *Meteorological Society*, 90, 1633-+, 10.1175/2009bams2804.1, 2009b.

851 Zhang, X. Y., Wang, Y. Q., Niu, T., Zhang, X. C., Gong, S. L., Zhang, Y. M., and Sun, J. Y.: Atmospheric aerosol
852 compositions in China: spatial/temporal variability, chemical signature, regional haze distribution and
853 comparisons with global aerosols, *Atmospheric Chemistry And Physics*, 12, 779-799, 10.5194/acp-12-779-
854 2012, 2012.

855 Zhang, Y., and Tao, S.: Global atmospheric emission inventory of polycyclic aromatic hydrocarbons (PAHs) for
856 2004, *Atmospheric Environment*, 43, 812-819, 10.1016/j.atmosenv.2008.10.050, 2009.

857 Zheng, B., Zhang, Q., Tong, D., Chen, C., Hong, C., Li, M., Geng, G., Lei, Y., Huo, H., and He, K.: Resolution
858 dependence of uncertainties in gridded emission inventories: a case study in Hebei, China, *Atmospheric*
859 *Chemistry And Physics*, 17, 921-933, 10.5194/acp-17-921-2017, 2017.

860 Zhong, J., Zhang, X., Wang, Y., Sun, J., Zhang, Y., Wang, J., Tan, K., Shen, X., Che, H., and Zhang, L.: Relative
861 contributions of boundary-layer meteorological factors to the explosive growth of PM 2.5 during the red-alert

862 heavy pollution episodes in Beijing in December 2016, *J. Meteorolog. Res.*, 31, 809-819, 10.1007/s13351-017-
863 7088-0, 2017a.

864 Zhong, J., Zhang, X., Wang, Y., Sun, J., Zhang, Y., Wang, J., Tan, K., Shen, X., Che, H., Zhang, L., Zhang, Z., Qi,
865 X., Zhao, H., Ren, S., and Li, Y.: Relative Contributions of Boundary-Layer Meteorological Factors to the
866 Explosive Growth of PM_{2.5} during the Red-Alert Heavy Pollution Episodes in Beijing in December 2016,
867 *Journal Of Meteorological Research*, 31, 809-819, 10.1007/s13351-017-7088-0, 2017b.

868 Zhong, J., Zhang, X., Dong, Y., Wang, Y., Liu, C., Wang, J., Zhang, Y., and Che, H.: Feedback effects of boundary-
869 layer meteorological factors on cumulative explosive growth of PM_{2.5} during winter heavy pollution episodes
870 in Beijing from 2013 to 2016, *Atmos. Chem. Phys.*, 18, 247-258, 10.5194/acp-18-247-2018, 2018a.

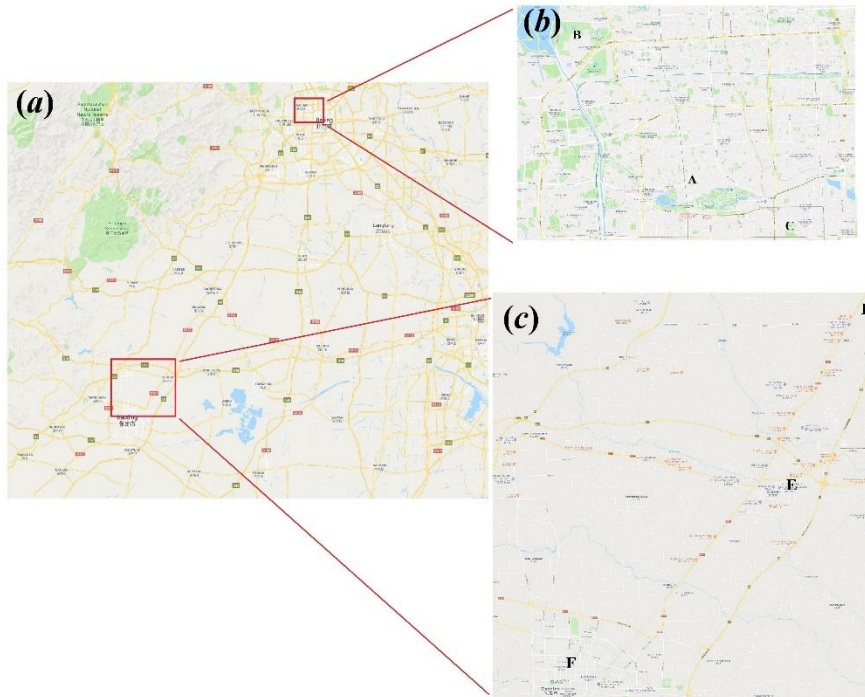
871 Zhong, J., Zhang, X., Dong, Y., Wang, Y., Liu, C., Wang, J., Zhang, Y., and Che, H.: Feedback effects of boundary-
872 layer meteorological factors on cumulative explosive growth of PM_{2.5} during winter heavy pollution episodes
873 in Beijing from 2013 to 2016, *Atmospheric Chemistry And Physics*, 18, 247-258, 10.5194/acp-18-247-2018,
874 2018b.

875 Zhong, J., Zhang, X., Wang, Y., Liu, C., and Dong, Y.: Heavy aerosol pollution episodes in winter Beijing enhanced
876 by radiative cooling effects of aerosols, *Atmos. Res.*, 209, 59-64,
877 <https://doi.org/10.1016/j.atmosres.2018.03.011>, 2018c.

878

879

880

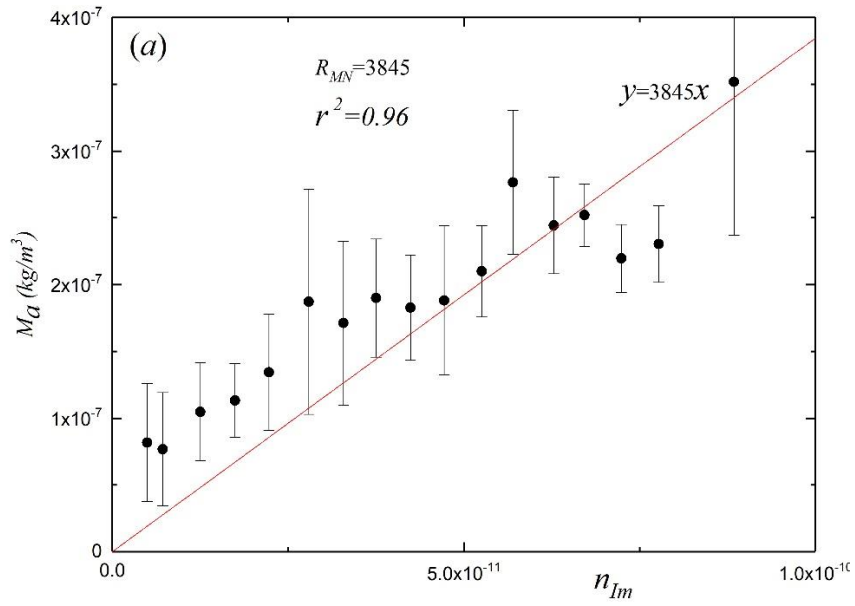


881

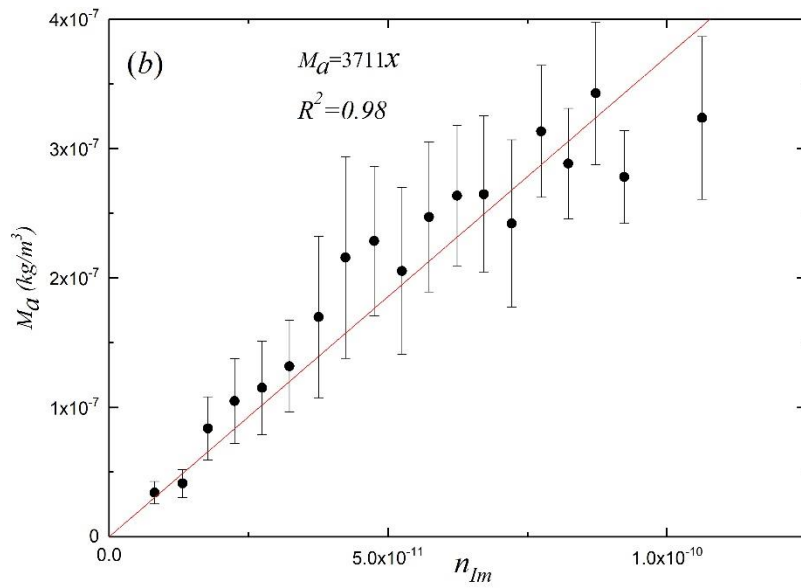


882

883 Figure 1. Photographs of the measurement site. (a) Map of the experiment area in the Beijing urban area
884 and suburban area and (b) expanded view of the Beijing experiment area, which is marked as the
885 rectangle in (a). (c) Expanded view of the Baoding experiment area, which is marked as the rectangle in
886 (a). (d) Satellite image of the CAMS site and (e) the satellite image of the GC site. Figs. 1a, b, c, and d
887 © Google.



888

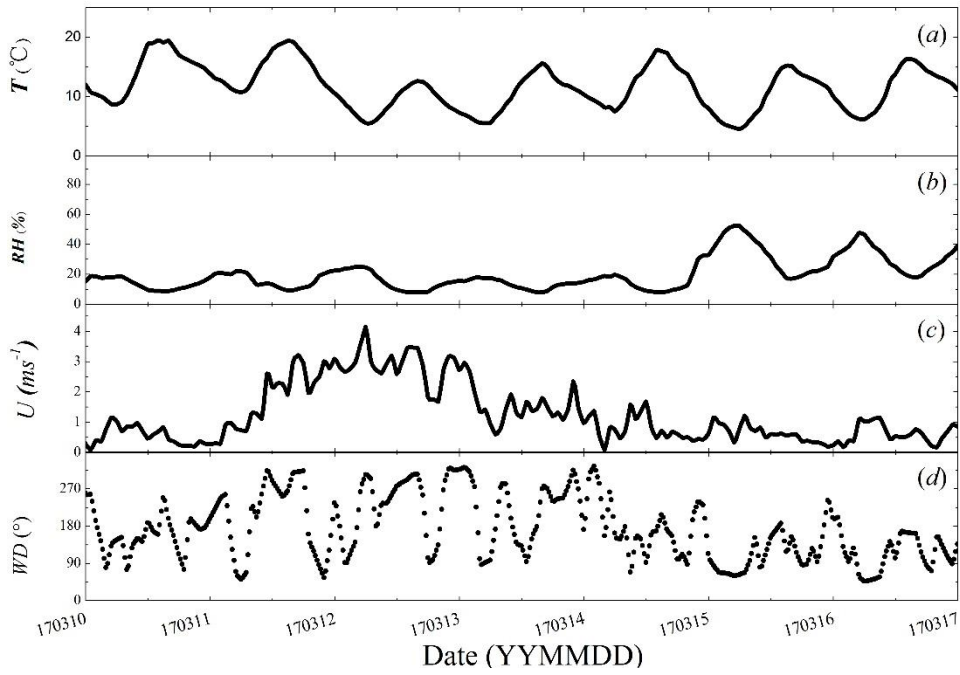


889

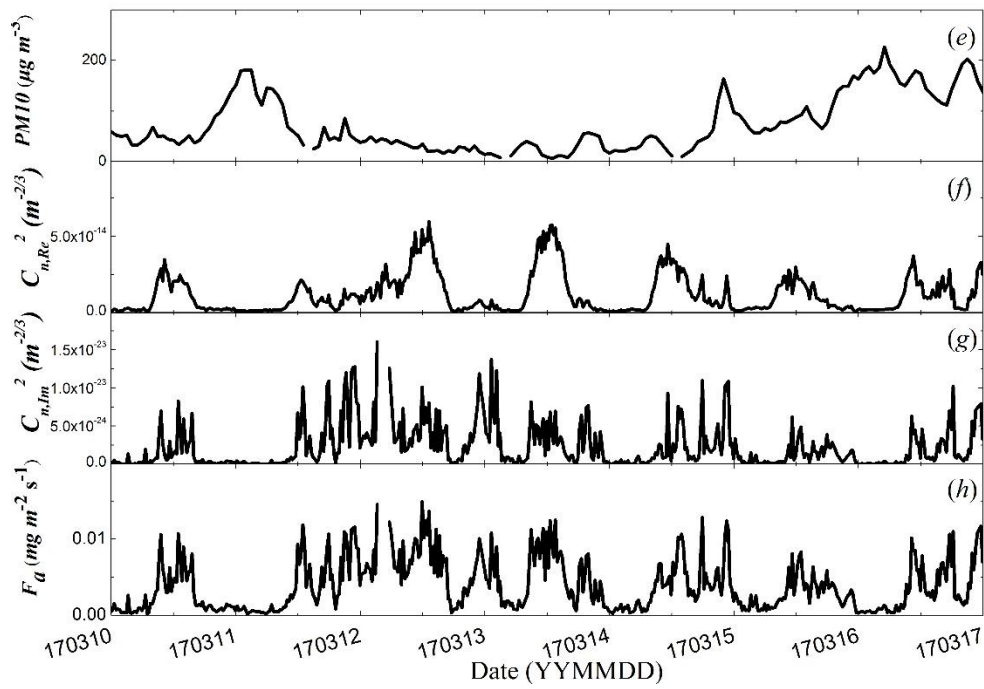
890

891 Figure 2. Relationship plot of aerosol mass concentration M_a and the imaginary part of the AERI for (a)

892 the Beijing area and (b) the Baoding area.

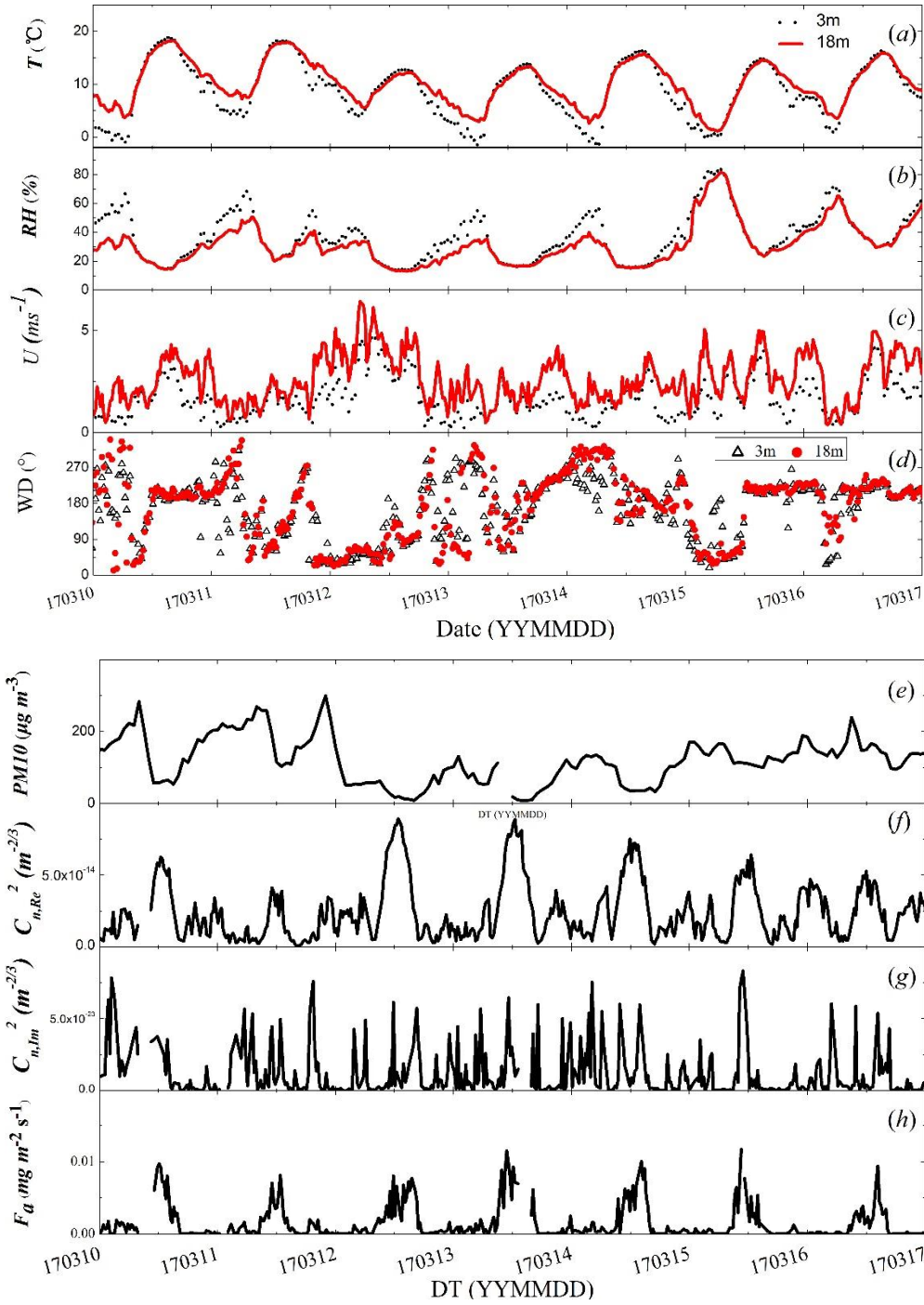


893



894

895 Figure 3. Temporal variations in (a) air temperature, (b) RH, (c) wind speed, (d) wind direction, (e) PM₁₀,
 896 (f) real part of the AERISP, (g) imaginary part of the AERISP and (h) aerosol mass flux in the Beijing
 897 area from March 10, 2017 to March 17, 2017.



898

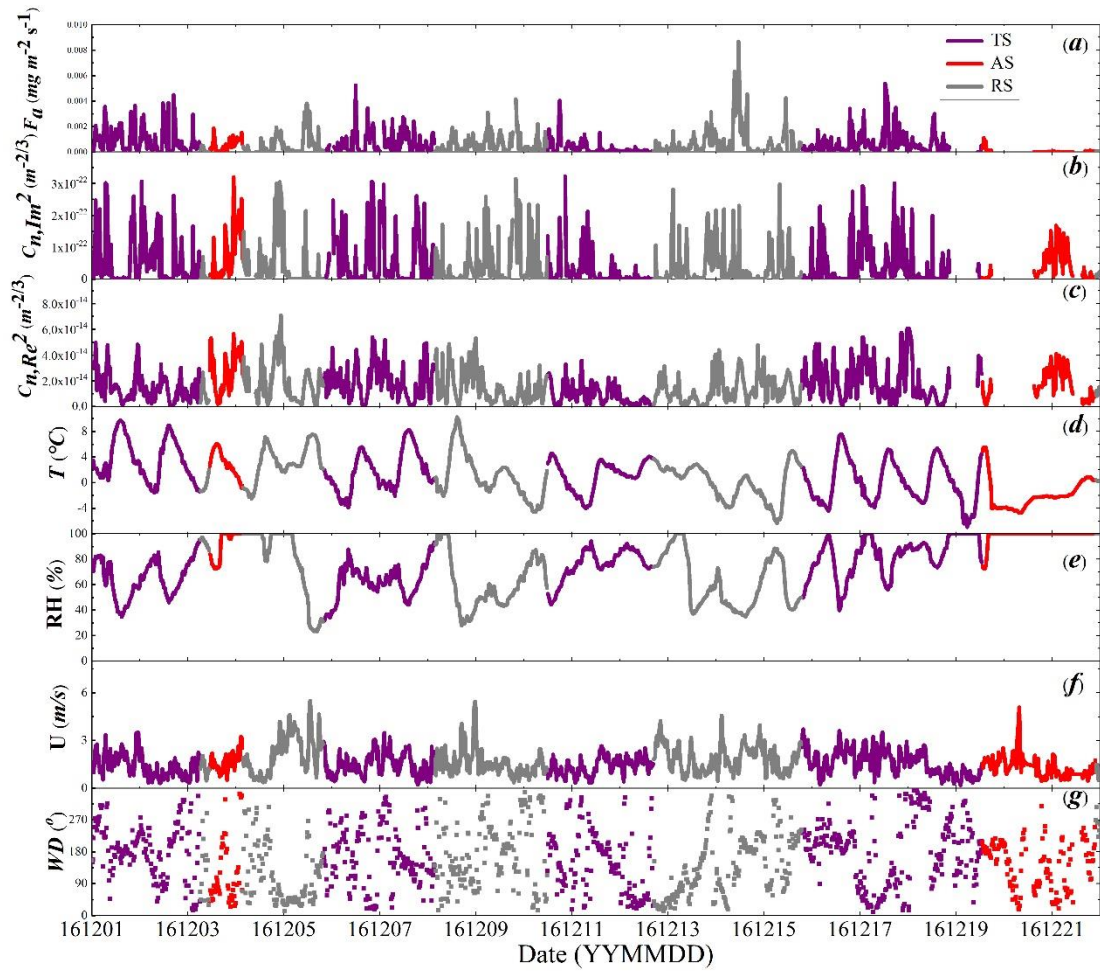
899

900 Figure 4. Temporal variations in (a) air temperature, (b) RH, (c) wind speed, (d) wind direction, (e) PM_{10} ,

901 (f) real part of the AERISP, (g) imaginary part of the AERISP and (h) aerosol mass flux in the Baoding

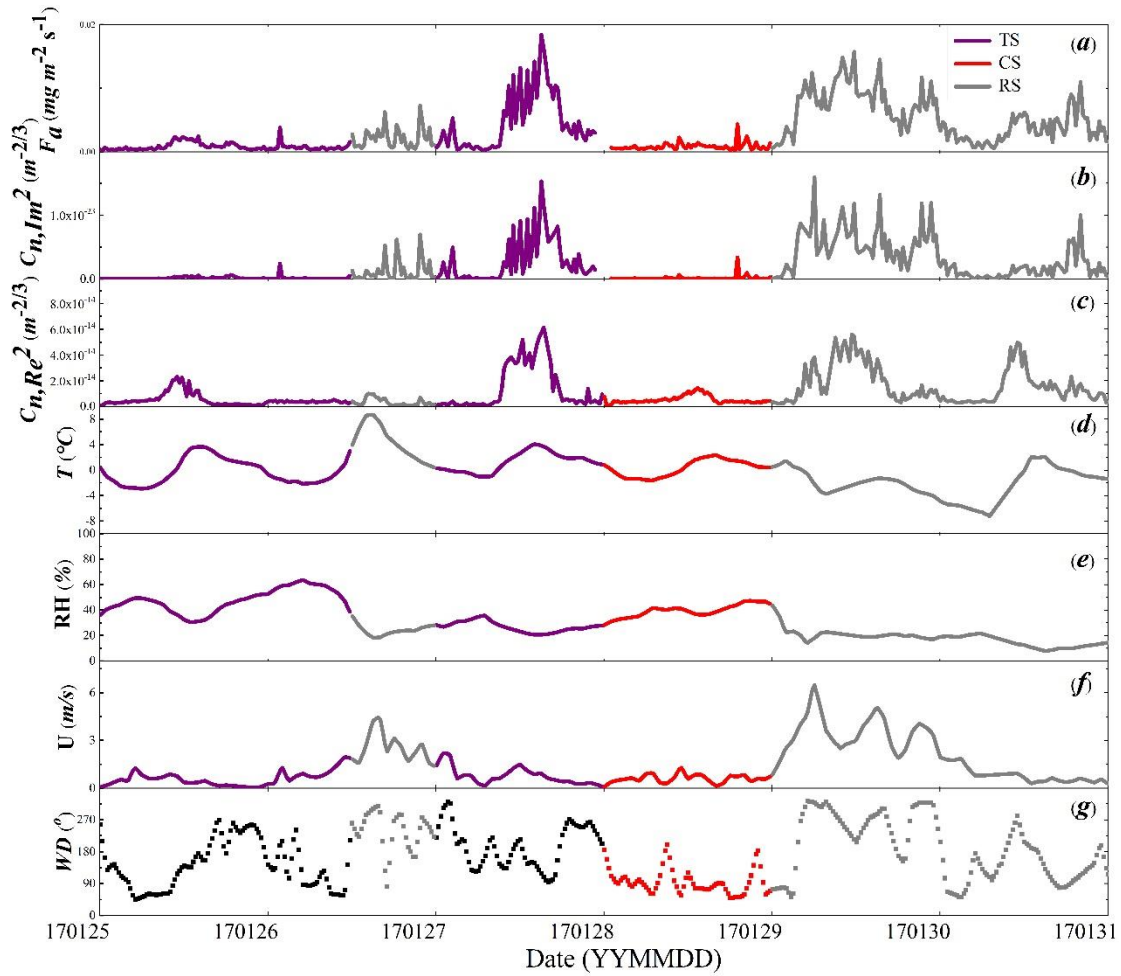
902 area from March 10, 2017 to March 17, 2017.

903



904

905 Figure 5. Temporal variations in (a) aerosol flux, (b) imaginary part of the AERISP, (c) real part of the
 906 AERISP (d) air temperature, (e) RH, (f) wind speed, and (g) wind direction in the Baoding area during a
 907 heavy pollution period, i.e., December 1, 2016 to December 22, 2016.



908

909 Figure 6. Temporal variations in (a) aerosol flux, (b) imaginary part of the AERISP, (c) real part of the
 910 AERISP (d) air temperature, (e) RH, (f) wind speed, and (g) wind direction in the Beijing area
 911 during a heavy pollution period, i.e., January 25, 2017 to January 31, 2017.

912